UNIVERSITY OF HELSINKI REPORT SERIES IN PHYSICS

HU-P-D167

Radiation effects in supported nanoparticles

Tommi Järvi

Division of Materials Physics
Department of Physics
Faculty of Science
University of Helsinki
Helsinki, Finland

ACADEMIC DISSERTATION

To be presented, with the permission of the Faculty of Science of the University of Helsinki, for public criticism in Auditorium D101 of the Department of Physical Sciences (Physicum), on November 6th, 2009, at 12 o'clock p.m.

HELSINKI 2009

ISBN 978-952-10-5638-3 (printed version)
ISSN 0356-0961
Helsinki 2009
Helsinki University Print (Yliopistopaino)

ISBN 978-952-10-5639-0 (PDF version)
http://ethesis.helsinki.fi/
Helsinki 2009
Electronic Publications @ University of Helsinki (Helsingin yliopiston verkkojulkaisut)

Tommi Järvi: **Radiation effects in supported nanoparticles**, University of Helsinki, 2009, 48 p.+appendices, University of Helsinki Report Series in Physics, HU-P-D167, ISSN 0356-0961, ISBN 978-952-10-5638-3 (printed version), ISBN 978-952-10-5639-0 (PDF version)

Classification (INSPEC): A7920N, A6185, A6170N, A6146
Keywords (INSPEC): nanoparticles, molecular dynamics method, ion beam effects

ABSTRACT

Nanotechnology applications are entering the market in increasing numbers, nanoparticles being among the main classes of materials used. Particles can be used, *e.g.*, for catalysing chemical reactions, such as is done in car exhaust catalysts today. They can also modify the optical and electronic properties of materials or be used as building blocks for thin film coatings on a variety of surfaces.

To develop materials for specific applications, an intricate control of the particle properties, structure, size and shape is required. All these depend on a multitude of factors from methods of synthesis and deposition to post-processing. This thesis addresses the control of nanoparticle structure by low-energy cluster beam deposition and post-synthesis ion irradiation.

Cluster deposition in high vacuum offers a method for obtaining precisely controlled cluster-assembled materials with minimal contamination. Due to the clusters' small size, however, the cluster-surface interaction may drastically change the cluster properties on deposition. In this thesis, the deposition process of metal and alloy clusters on metallic surfaces is modelled using molecular dynamics simulations, and the mechanisms influencing cluster structure are identified. Two mechanisms, mechanical melting upon deposition and thermally activated dislocation motion, are shown to determine whether a deposited cluster will align epitaxially with its support.

The semiconductor industry has used ion irradiation as a tool to modify material properties for decades. Irradiation can be used for doping, patterning surfaces, and inducing chemical ordering in alloys, just to give a few examples. The irradiation response of nanoparticles has, however, remained an almost uncharted territory. Although irradiation effects in nanoparticles embedded inside solid matrices have been studied, almost no work has been done on supported particles. In this thesis, the response of supported nanoparticles is studied systematically for heavy and light ion irradiation. The processes leading to damage production are identified and models are developed for both types of irradiation.

In recent experiments, helium irradiation has been shown to induce a phase transformation from multiply twinned to single-crystalline nanoparticles in bimetallic alloys, but the nature of the transition has remained unknown. The alloys for which the effect has been observed are CuAu and FePt. It is

shown in this thesis that transient amorphization leads to the observed transition and that while CuAu and FePt do not amorphize upon irradiation in bulk or as thin films, they readily do so as nanoparticles. This is the first time such an effect is demonstrated with supported particles, not embedded in a matrix where mixing is always an issue.

An understanding of the above physical processes is essential, if nanoparticles are to be used in applications in an optimal way. This thesis clarifies the mechanisms which control particle morphology, and paves way for the synthesis of nanostructured materials tailored for specific applications.

Contents

1 INTRODUCTION

In the past few decades, materials science research has moved more and more towards examining nanostructured materials. Being on the border between atomic and macroscopic worlds, nanosized systems exhibit many intriguing properties that arise mainly from two physical effects. First, in small structures the quantization of electronic states becomes apparent, leading to a very sensitive size dependence of optical and magnetic properties. Second, the high surface-to-volume ratio alters the thermal and mechanical properties of materials, introducing a size dependence to most material properties. Thus, while 1 and 2 mm pieces of gold certainly have very similar physical properties, this is no longer the case for pieces of 10 and 20 nm.

In some cases size-dependent phenomena have been known for a long time. An example is the melting point depression of small clusters, for which a size-dependence was predicted by Pawlow already in 1909 [1]. However, the properties of nanomaterials have already been used much earlier, albeit unknowingly. One of the most famous examples is the Lycurgus cup from around the fourth century A.D. [2] The cup is green in direct light but with light shining through the glass, it turns into a translucent red colour. The glass contains small (50–100 nm) particles of gold-silver alloy with some copper in them, causing the beautiful colours. Another example of ancient use of nanotechnology is the steel of Damascus blades, believed to be produced in ancient India, which had superior properties as compared to other steels of the time. Indeed, carbon nanotubes and cementite nanowires have been found in the steel [3].

It is, however, only with the development of advanced experimental techniques in the past few decades that one has really been able to start exploring the wealth of phenomena occurring at the nanoscale and to understand how the structures and sizes of nano-objects relate to their properties. Atomic scale resolution can nowadays be achieved with for example transmission electron microscopy [4], allowing the study of individual nano-objects, and methods exist even for detecting single chemical reactions in real time [5]. Thus the current and potential applications of nanotechnology are quickly increasing in number.

The field where nanotechnology is perhaps most used today is catalysis. There, nanoparticles are used to turn harmful hydrocarbons in car exhaust fumes into carbon dioxide and other bening species. They are also used to catalyse the growth of single-walled carbon nanotubes [6]. Other on-the-market applications include reinforcing and boosting the thermal and electrical conductivities of epoxies with carbon nanotubes [7], modifying the optical properties of glasses with nanoparticles, and allowing the manufacture of coatings for a variety of applications on almost any material [8].

For nanoparticles, the subject of this thesis, most applications rely on either individual clusters or cluster-assembled thin films being supported on some kind of a substrate. Because of the small size of the particles the cluster-substrate interaction may cause drastic changes in the particle shape. Understanding how clusters interact with substrates is thus of primary importance. For example, the catalytic activity of platinum particles depends sensitively not only on their size but also on their shape [9]. The same is true for the performance of silver particles in molecular recognition [10].

Besides the manufacturing process, also post-synthesis methods can be used to control the properties of materials. A method very commonly used in the semiconductor industry is ion irradiation. It is used for doping and etching, smoothing and patterning of surfaces, inducing ordering in alloys, and for a variety of other purposes [11–15]. The use of irradiation to modify nanosized objects is in contrast a field where in terms of possible uses, only the surface has hitherto been scratched.

The studies presented in this thesis aim at understanding the deposition of nanoparticles on substrates and the response of nanoparticles to ion irradiation, to enable post-synthesis modification of their properties. Regarding ion irradiation, the behaviour of supported particles upon irradiation is an almost uncharted territory, and indeed interesting phenomena not akin to those in bulk are found. With the development of methods to accurately control nanoparticles' shapes and sizes, it will be possible to tailor catalysts and other materials for specific applications, and to use a minimal amount of material to achieve the desired effect.

2 PURPOSE AND STRUCTURE OF THIS STUDY

The purpose of this thesis is to understand how the structure of nanoparticles can be controlled using ion irradiation, and what mechanisms determine the structure of particles deposited from the gas phase onto supporting surfaces. More specifically, the following questions were considered:

- What mechanisms determine whether deposited clusters align epitaxially with their support?
- How do nanoparticles respond to ion irradiation? What are the differences to bulk?
- What kind of phase transformations can ion irradiation induce in nanoparticles? What are the atomistic mechanisms?

This thesis consists of this summary and six publications, published in peer-reviewed international journals. The six publications are referred to by boldface Roman numerals and are summarized in this section. The summary also includes results from other articles, some by the author [16–19].

This summary consists of seven sections. In this section, the publications are summarized and the author's contribution explained. Section 3 introduces the main subject of this thesis, nanoparticles and their structure and properties. The methods of simulation are outlined in section 4. The main results are discussed in sections 5 and 6. Section 5 is devoted to low energy cluster beam deposition and irradiation effects in nanoparticles are discussed in section 6. Finally, conclusions are presented in section 7.

2.1 Summaries of the original publications

In publication **I**, the deposition of metallic nanoparticles is studied and the physical processes that determine whether epitaxial alignment is achieved are identified. In publication **II**, the study is extended to nanoalloys and the extent to which alloy disordering occurs is investigated.

Publications **III**–**VI** concern the response of nanoparticles to ion irradiation. Systematic size dependencies of damage production under heavy and light ion bombardment are established in publications **III** and **IV**. Publication **V** maps the possible structural transitions in metallic nanoparticles as a result of heavy and light ion bombardment. In publication **VI**, experiments showing a phase transformation from multiply twinned to single-crystalline nanoparticles upon helium irradiation are presented. Based on molecular dynamics simulations, the transition pathway is proposed to involve transient amorphization of the alloyed particles, the alloys being ones that do not amorphize in bulk.

Publication I: Contact epitaxy by deposition of Cu, Ag, Au, Pt, and Ni nanoclusters on (100)-surfaces: Size limits and mechanisms,
T. T. Järvi, A. Kuronen, K. Meinander, K. Albe, and K. Nordlund, *Physical Review B* **75**, 115422 (2007).

The deposition of metallic nanoparticles on metallic substrates is studied to identify the mechanisms determining whether deposition occurs epitaxially or not. Two processes are shown to dominate epitaxial alignment. At small cluster sizes, the surface energy released from the particle-substrate interface heats the cluster. Mechanical, or homogeneous, melting occurs for clusters that are smaller than a critical size, enabling epitaxial alignment. For larger particles, and extended time scales, thermally activated dislocation motion is shown to promote epitaxiality.

Publication II: Low energy cluster deposition of nanoalloys,
T. T. Järvi, A. Kuronen, K. Nordlund, and K. Albe, *Journal of Applied Physics* **106**, 063516 (2009).

The study of publication **I** is extended to alloyed clusters. The same mechanisms are shown to govern epitaxial alignment as for elemental clusters. $L1_2$ ordered alloy particles are used to quantify the disordering occurring upon deposition and a simple phenomenological model is derived for its size dependence. A single expression for the critical particle size for epitaxial alignment, resulting from the mechanical melting and dislocation mechanisms introduced in publication **I**, is derived.

Publication III: Enhanced sputtering from nanoparticles and thin films: Size effects,
T. T. Järvi, J. A. Pakarinen, A. Kuronen, and K. Nordlund, *EPL* **82**, 26002 (2008).

The response of gold nanoparticles of different sizes and thin films of different thicknesses on 25 keV Ga irradiation is studied to establish a size dependence of the sputtering yield. Yield enhancements up to a factor of four as compared to bulk irradiation are observed for nanoparticles. The results are explained in terms of an analytical model based on Sigmund's sputtering theory.

Publication IV: Damage production in nanoparticles under light ion irradiation,
T. T. Järvi, A. Kuronen, K. Nordlund, and K. Albe, *Physical Review B (Brief Reports)* **80**, 132101 (2009).

Irradiation of metals and semiconductors by light ions, such as helium, creates mainly point defects in the form of Frenkel pairs. In this publication, a systematic size dependence of sputtering and defect production in metallic (Pt) nanoparticles upon He irradiation is established. It is shown that, contrary to what is observed for heavy ion irradiation in publication **III**, the sputtering yield does not depend on particle size. On the other hand, the maximal vacancy concentrations are shown to increase with particle diameter for the studied range of 2–5 nm, leading to concentrations higher than in bulk. A rate equation based model is developed and is shown to describe the irradiation-induced processes.

Publication V: Structural modification of a multiply twinned nanoparticle by ion irradiation: A molecular dynamics study,
T. T. Järvi, A. Kuronen, K. Nordlund, and K. Albe, *Journal of Applied Physics* **102**, 124304 (2007).

In this publication, the effects of light and heavy ion irradiation on the structure and morphology of nanoparticles are investigated. Circa 4 nm multiply twinned platinum nanoparticles are irradiated with 1–10 keV He and Xe ions. The target nanoparticles are unsupported, mimicking in-flight irradiation, or irradiation on weakly interacting substrates. Helium irradiation is shown to only lead to Frenkel pair production, while no change in the grain boundary content of the particle is observed, contrary to experimental evidence for FePt particles. This discrepancy is explained in publication **VI**. Xenon

irradiation is shown to lead to extensive damage. It is demonstrated that a single ion hitting the particle can lead to complete or partial melting.

Publication VI: From multiply twinned to fcc nanoparticles via irradiation-induced transient amorphization,
T. T. Järvi, D. Pohl, K. Albe, B. Rellinghaus, L. Schultz, J. Fassbender, A. Kuronen, and K. Nordlund, *EPL* **85**, 26001 (2009).

Experimental evidence is presented for a phase transformation, where multiply twinned CuAu nanoparticles turn single-crystalline upon helium irradiation. This is surprising as He irradiation is only expected to cause Frenkel pair formation (see publications **IV** and **V**). Molecular dynamics simulations indicate that the alloyed nanoparticles amorphize under irradiation, something that the corresponding bulk alloys do not do. A transformation pathway from multiply twinned to single-crystalline morphology is proposed, based on the amorphization and simultaneous recrystallization.

2.2 Author's contribution

The author carried out all of the simulations in publications **I**–**VI** except for publication **III**, where he supervised a part. Analysis of the results and writing the manuscripts was mainly done by the author for all publications. The experimental work for publication **VI**, and writing the corresponding part of the manuscript, was done by the Metastable and Nanostructured Materials group at IFW Dresden and Dr. Fassbender at Forschungszentrum Dresden-Rossendorf.

3 NANOPARTICLES

Nanostructures can be roughly categorized in terms of how many of their dimensions are macroscopic. Two-dimensional structures, thin films, have one nanoscopic dimension, while carbon nanotubes and nanowires are examples of one-dimensional nanostructures. Nanoparticles, or nanoclusters, which are the subject of this thesis, have no macroscopic dimensions. The word nanocluster is often defined as an agglomerate consisting of identical subunits that may be atoms but also molecules or other entities, while the word nanoparticle is not equally precisely defined. The two are used synonymously in this thesis meaning particles composed of atoms.

There are several ways to produce nanoparticles. Chemical methods may be used to obtain them in solution, often leading to particles protected by ligands. An archetypal example is thiol-protected gold

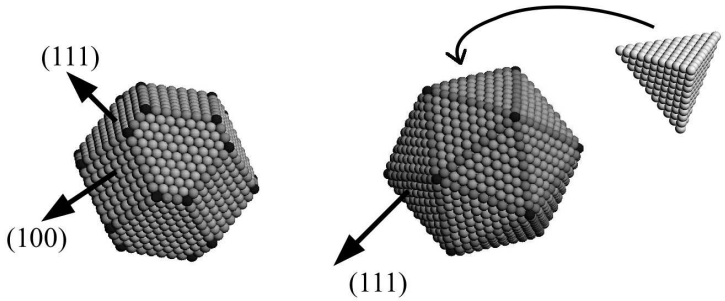

Figure 1: Single-crystalline nanoparticles (left) are small pieces of bulk matter, while multiply twinned icosahedral nanoparticles (right) contain grain boundaries at the interfaces between their tetrahedral parts.

clusters produced by the Brust-Schiffrin reaction [20]. Ion beams can be used to implant atoms into solid matrices, the atoms subsequently agglomerating into embedded nanoparticles [21]. Embedded particles can also be produced by other means, *e.g.*, co-deposition [22]. The method most relevant to the studies in this thesis is to produce particles by aggregation from atomic vapour in an inert gas condensation source [8]. The particles can then be deposited on a substrate in vacuum, avoiding oxidation and other contamination.

3.1 Structures and shapes of nanoparticles

Nanoparticles come in various structures and morphologies. While this thesis concentrates on nanoparticles made of metals and alloys with the face-centered cubic (fcc) structure, most of the discussion below also holds, sometimes with minor modifications, for other systems, for example semiconducting materials or materials with other crystal structures.

Ignoring entropic effects, the energetics of clusters is an interplay between the bulk and surface parts of the particle. Two typical structures for small metal particles are illustrated in Fig. 1. The one on the left is simply a small piece of the corresponding bulk material. For most materials, the surface facets of such a particle are determined by the Wulff construction, which, in simplified terms, states that the area of a particular facet is inversely proportional to its surface energy [23–25]. The particle on the right is a multiply twinned icosahedron that only has (111) facets. This minimizes surface energy. However, the reason the icosahedron is not always the lowest energy structure is that it both contains grain boundaries in its bulk and is strained. This is because it is composed of tetrahedral subunits that cannot match perfectly at the interfaces. Therefore, the icosahedron is usually the ground state at smaller sizes while the Wulff polyhedron dominates for larger particles. Ref. [26] provides an excellent overview of structures and energetics of nanoparticles of varying shapes.

For very small clusters, below approximately 100 atoms, there is an additional effect influencing the structure. For these particles the closing of electronic and geometric shells leads to so called magic numbers that are more stable than other nearby cluster sizes [27, 28]. This demonstrates an important feature: For very small particles, even adding, removing or changing a single atom may lead to significant changes in cluster properties [25]. For example, the effect of impurities can be much stronger as compared to bulk, a single copper atom in an $Al_{\sim 50}$ cluster modifying the cluster's melting behaviour significantly [29].

Since nanoparticles often have isomers that are almost equal in energy, entropic effects become important [25]. For instance, particles can exhibit solid-solid phase transformations at high temperatures before melting [30] and may support statically or dynamically co-existing liquid and solid phases [31].

3.2 Size-dependent properties

The most interesting feature of nanoparticles, both scientifically and from an application point of view, is that many of their properties depend sensitively on particle size. The most common example is the optical spectrum of semiconductor nanoparticles, such as CdSe [32, 33]. Their photoluminescence colour can be tuned from blue to red by simply changing the particle size, with no need for chemical modification.

An equally well-known size effect is the depression of melting point, already predicted by Pawlow in 1909 [1, 25, 34]. However, for very small particles (a few tens of atoms) of Sn and Ga, melting points higher than for bulk have been reported [25, 35, 36]. The former case is due to the pronounced disordering of surface atoms, while the mechanisms leading to the latter are less well known. The increasing covalent character of bonds with decreasing cluster size is one possible explanation [37].

Also other properties change with decreasing particle size. The solid solubilities in alloyed particles depend on size [38]. Defect formation energies increase with decreasing particle size, leading to lowered equilibrium vacancy concentrations in metal nanoparticles [39–41]. In contrast, the *non-equilibrium* vacancy concentrations that can be obtained using ion irradiation are higher in nanoparticles compared to bulk systems [**IV**]. Also, sputtering yields under cascade-producing irradiation can be enhanced as much as fourfold, depending on particle size [**III**], whereas for irradiation in the single knock-on regime, no enhancement is observed [**IV**].

Size-effects are equally important for cluster-assembled and nanocrystalline materials. For polycrystalline materials, an increase in hardness is observed with decreasing grain size, displaying the so-called Hall-Petch effect [42–44]. However, for very small grain sizes (below 10 nm) an inverse

Hall-Petch relation may lead to decreasing hardness [45]. Similar size effects on hardness are also observed for individual nanoparticles [46–48].

4 METHODS

Ever since computers began to be powerful enough to run practical calculations, the traditional scientific arts of experiment and theoretical calculation have been accompanied by computational science. The role of simulation has in the past one to two decades grown immensely along with ever-increasing computational power, simulations sometimes being called experiments *in silico*. With powerful parallel computers, it is nowadays possible to simulate systems containing hundreds of millions of atoms by classical molecular dynamics, and conversely, to calculate properties of hundreds of atoms directly from quantum mechanics. Besides predicting new phenomena, simulation is also a useful tool for explaining experimental results, where processes occur on such length and time scales that are not directly accesible by measurement.

The major part of this thesis concerns classical molecular dynamics simulations, but also results from experiments, carried out by collaborators, are presented in publication **VI**.

4.1 Molecular dynamics simulation and interatomic potentials

In its simplicity, the molecular dynamics (MD) method is based on solving classical equations of motion for a system consisting, usually, of atoms. Given initial atom positions and velocities, forces are solved from an interaction model and the equations of motion are integrated over a small time step. The basic methodology is introduced in, *e.g.*, Refs. [49–51]. The simulations in this thesis were carried out with the PARCAS code written mostly by Kai Nordlund [52–54].

The molecular dynamics method is based on the Born-Oppenheimer approximation [55], whereby it is assumed that the electronic degrees of freedom relax fast enough, so that only their ground state potential energy surface is relevant from the point of view of atomic motion. Within this approximation, it is possible to solve the forces using *ab initio* methods, for example density functional theory (DFT) [51]. This approach is only useful for small systems and short time scales though, due to the large amount of computing necessary for solving the electronic structure.

Instead, and this is the only (though major) approximation in the method, a classical model potential is usually used, from which the forces are calculated. There are several such potentials from non-reactive molecular mechanics force fields [56] to reactive potentials [57–60]. Besides pair potentials,

two potential types are used in this thesis, the embedded-atom-method (EAM) [61, 62] and bond-order [59] potentials.

Pair potentials give the system energy as a sum of pairwise interactions (ϕ),

$$E_{\text{pair}} = \frac{1}{2} \sum_{\substack{i,j=1 \\ i \neq j}}^{N} \phi_{ij}(r_{ij}), \tag{1}$$

where i and j sum over all atoms and r_{ij} is the distance between atoms i and j. In this thesis, pair potentials are used for the interactions between bombarding ions and the target atoms. In that case, significant many-body effects are not expected, because instead of a chemical reaction, the ion transfers energy to the target atoms by collisions.

The embedded-atom-method is often used for metallic elements and alloys. It is inspired by DFT, the energy of a system with N atoms being given by [62]

$$E_{\text{EAM}} = \frac{1}{2} \sum_{\substack{i,j=1 \\ i \neq j}}^{N} \phi_{ij}(r_{ij}) + \sum_{i=1}^{N} F_i(\rho_i); \qquad \rho_i = \sum_{\substack{j=1 \\ j \neq i}}^{N} \rho_{ij}(r_{ij}), \tag{2}$$

where the first term is a pairwise interaction (ϕ) between the atoms and the second one corresponds to the energy required to embed an atom in the combined electron density (ρ) of its neighbours, giving rise to the many-body character of the potential.

A bond-order potential also consists of two terms [59, 63],

$$E_{\text{BO}} = \frac{1}{2} \sum_{\substack{i,j=1 \\ i \neq j}}^{N} \left[A e^{-\lambda r_{ij}} - b_{ij} B e^{-\mu r_{ij}} \right], \tag{3}$$

a repulsive and an attractive one. The attractive term is multiplied by the bond-order parameter b through which the many-body character of the potential appears. The bond-order usually also contains angular contributions. Bond-order potentials have succesfully been applied for both semiconductors and metals, as well as ionic compounds [59, 63–68].

The potentials used the most in this thesis are the EAM potentials for Au, Ag, Cu, Ni and Pt, and their alloys, by Foiles *et al.* [69], used in publications **I–III** and **VI**, and the bond-order potentials for Fe, Pt, and FePt by Müller *et al.* [70, 71], used in publications **IV–VI**.

4.2 Simulation of high energy phenomena

The phenomena studied in this thesis are intrinsically far from thermodynamic equilibrium. This is especially true for ion irradiation, where kinetic energies up to hundreds of MeV's can be present. Conventional molecular dynamics simulation, and interatomic potentials, are geared towards simulating near-equilibrium systems, and several additional factors need to be taken into account when higher energy processes are simulated. The most important ones are reviewed below.

First, since high energy atoms imply high velocities, a very small time step for integrating the equations of motion is required. Usually a constant step is used in molecular dynamics. However, as high energy atoms slow down fast, keeping the same time step for the entire simulation would waste a lot of computing power. Thus an adaptive time step is used that makes sure that no atom moves too much during a single step, and that as the system approaches equilibrium, the step increases [52].

As a high energy atom travels through matter, not only does it lose energy by collisions with other atoms, but also due to electronic excitations [72]. Because molecular dynamics treats electronic degrees of freedom in a completely effective manner, there is no rigorous way to take this electronic stopping into account. Fortunately, as also required for the Born-Oppenheimer approximation to hold, the electron system equilibrates on a much faster time scale than it couples with ionic motion. In metals the situation is also alleviated by the fact that no charge build-up occurs. Because of this, the ions, to a very good approximation, see electronic stopping as a friction-like force [72]. This is easily accomodated by adding a velocity-dependent force to the equations of motion of atoms with kinetic energies higher than a certain threshold, usually 1–5 eV. Although more intricate methods exist, this approach is quite adequate, and simple to implement [73].

Finally, the interatomic potentials may also need to be modified to properly simulate high energy events. Fig. 2 shows a schematic pair potential between two atoms. Most interatomic potentials are designed to describe systems close to equilibrium and thus the well of the potential is well described. However, as atoms get closer to each other and reach higher energies, a realistic description is no longer guaranteed. Some potentials even reach a constant value at zero distance (as in Fig. 2), or are not defined at all beyond a certain energy. Hence clearly the short-range part has to be always tested and usually modified.

A good description of the repulsive interaction between atoms can be obtained for example from *ab initio* calculations. Another possibility, used in most of the publications of this thesis, is to use the universal, purely repulsive Ziegler-Biersack-Littmark (ZBL) pair potential [72]. This is an analytic

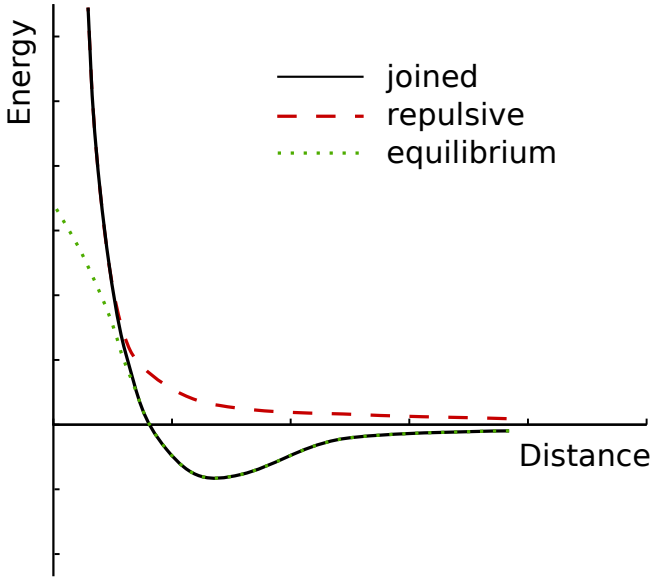

Figure 2: For high energy applications, the equilibrium potential has to be replaced by a realistic short-range repulsive interaction.

approximation based on a screened Coulomb interaction between the nuclei,

$$E_{\mathbf{ZBL}} = \frac{e^2}{4\pi\varepsilon_0}\frac{Z_1 Z_2}{r}\phi(\frac{r}{a_U}), \tag{4}$$

where best universality is achieved with the screening function

$$\phi(x) = 0.1818\,e^{-3.2x} + 0.5099\,e^{-0.9423x} + 0.2802\,e^{-0.4028} + 0.02817\,e^{-0.2016x}, \tag{5}$$

and reduced length $a_U = 0.8854\,a_0/(Z_1^{0.23} + Z_2^{0.23})$, a_0 being the Bohr radius [72].

The repulsive potential is splined to the equilibrium potential over some interval, as shown schematically in Fig. 2. After making sure that no spurious minima are introduced, the combined potential can be used for more realistic simulation of high energy processes, while preserving all the equilibrium properties of the original potential. The joining of the potentials can also be used to fit intermediate-energy properties, for example the threshold displacement energy [74].

The ZBL potentials can also be used for the interaction between the incoming ion and the target atoms, as the missing attractive part is not essential in irradiation processes, where the ions do not react chemically with the target, but transfer energy by collisions.

4.3 Simulation setup

The setup and analysis of the different simulations done for this thesis are explained in detail in the corresponding publications. Here the essential features are reviewed for the most typical cases, *i.e.*, cluster deposition and ion irradiation.

When simulating cluster deposition, the substrate and the impacting cluster were first separately equilibrated, after which the cluster was randomly rotated, and translated within $[-a,a]$ in the lateral directions, a being the lattice constant. The cluster was then placed above the substrate and given a velocity towards it. A few bottom layers of the substrate were fixed to simulate bulk matter and periodic boundary conditions were applied in the lateral directions. The temperature control method of Berendsen *et al.* [75] was used to keep a few atomic layers at ambient temperature at the periodic boundaries as well as above the fixed atoms at the bottom of the cell. The rest of the atoms were simulated in the NVE ensemble. The temperature controlled region served as a heat sink emulating the effect of heat conduction away from the region of interest.

The simulations were continued for 2 ns in the case of publications **I** and **II**. To determine whether an epitaxial configuration was reached, the simulation trajectories were inspected mainly visually.

To compare against the irradiation response of nanoparticles, ion irradiation of bulk surfaces was simulated in publications **III–V**. These simulations were conducted similarly to the cluster deposition simulations described above, except that instead of the cluster, an impinging ion was placed above the surface in the beginning of the simulation. A large target surface was necessary for ions with high energy, as according to an often-used rule of thumb, one needs around 10000 target atoms to disperse 1 keV of impinging kinetic energy. This prevents artifacts caused by shock waves or high energy atoms from reaching the cell boundaries.

In publication **III**, also irradiation of thin films was studied. This was carried out similarly to other surface irradiation simulations, except that the bottom of the film was not fixed, and temperature control was only applied at the periodic, lateral boundaries.

Ions impinging on nanoparticle targets were studied in publications **III–VI**. In these cases the particle was initially equilibrated and, depending on the case, randomly rotated before the impacting ion was placed above it. The ion was allowed to impact with a random impact parameter chosen inside a radius given by a cylinder wrapped around the cluster. No temperature control was used during the simulations but for simulating successive ion impacts on a single particle, the particle was cooled to ambient temperature between impacts.

The target nanoparticles were placed in vacuum in all simulations. This corresponds to irradiation on a weakly interacting substrate such as amorphous carbon or graphite. To explicitly include for example a carbon substrate would increase computing time considerably because of the increased number of atoms, and because carbon as a light element requires a small time step to be used in integrating the equations of motion.

4.4 Analysis methods

Several methods were used in the analysis of the simulation results. An analysis code was developed by the author for this purpose [76]. Automatic analysis was required for determining the sputtering yield and vacancy production as well as for assigning atoms to different classes based on their environment.

For determining sputtering yields, a clustering algorithm was used. Atoms were grouped into clusters based on a pre-defined cutoff distance, and the largest cluster, corresponding to the damaged target, was exluded when determining the sputtered atoms and clusters.

Analysing vacancy production in nanoparticles is complicated by the fact that the particles' center-of-mass may move and they may rotate due to the ion impact. Thus methods based on counting the number of atoms in each Wigner-Seitz cell of the perfect lattice fail [77]. Instead, we used a method of searching for free space inside the particles in the form of spheres. Spheres with a radius of 0.8 times the nearest neighbour distance were found to yield very reliable vacancy counts in publications **IV** and **V**. After filling all empty space in the system with the spheres, a clustering algorithm was used to identify and remove the largest vacancy cluster, which corresponds to the vacuum outside the nanoparticle. This method has the additional advantage that surface roughness is treated automatically.

For structural analysis, two methods were used. To identify atoms belonging to different crystal structures such as fcc atoms or atoms at grain boundaries, common neighbour analysis was employed [78]. This method assigns an identifying number for each pair of atoms according to whether the atoms are neighbours, how many common neighbours they have, and in what way their common neighbours are each other's neighbours. Whether atoms are neighbours or not is determined by a cutoff distance. Each atom may then be classified according to the pair types it forms with other atoms.

For separating solid and disordered or liquid atoms in publications **II** and **V**, and crystalline and amorphous atoms in publication **VI**, the method described in Ref. [79] was used. This method is

based on bond correlation using spherical harmonics, and was here used with the modification that in place of the correlation function c_{ij} (see Ref. [79]), its absolute value was used.

5 CLUSTER DEPOSITION

Cluster deposition in high vacuum conditions is a common way to create nanostructures with little oxidation or other contamination of the materials [8, 80]. It can be used for depositing separated particles or for manufacturing for example cluster-assembled thin films [81]. Cluster deposition has several advantages as compared to traditional single-atom deposition methods. With energetic cluster impacts, very high energy densities can be deposited in small target areas, causing crater formation and implantation of the cluster into the target [18]. One important advantage of cluster ion beams is that the mass transported per current density is very high [82]. This is simply because the ions in a cluster beam contain up to thousands of atoms instead of just one, as is the case with a conventional ion beam. On one hand, this means that for an ion beam of given current density, high deposition rates can be obtained. On the other hand, space charge effects make it difficult to deposit monomer ions at low energies [82]. No such problem exists for nanoclusters, as the kinetic energy is divided among the cluster atoms. Thus each individual atom has a very low kinetic energy even when the total energy of the cluster is high. This allows deposition without damaging the substrate, as well as very shallow implantation currently used in semiconductor technology [82, 83]. Clusters can even be made to reflect from the target surface [84], allowing site-selective deposition [85].

5.1 Cluster deposition regimes

A phase diagram-like description of different cluster deposition regimes is presented in Fig. 3 for the case of Au clusters on Au [18]. Depending on the impacting cluster's size and energy, different deposition regimes can be distinguished. For low energies, the cluster remains at the target surface. If the deposition energy is high enough and the cluster small enough, the cluster can align epitaxially with the substrate. As impact energy is increased, the cluster penetrates deeper into the target. In dense materials such as Au, a heat spike is formed, and if the cluster range is not too high, most of the energy is deposited near the surface, leading to cratering by liquid flow. Further increasing the energy leads to implantation.

For larger impactor sizes, the energy window for epitaxial deposition and liquid flow cratering becomes narrower. Increasing the impactor energy and size ultimately leads to macroscopic cratering behaviour very much like that for meteorites impacting on the moon. For Au particles on Au and

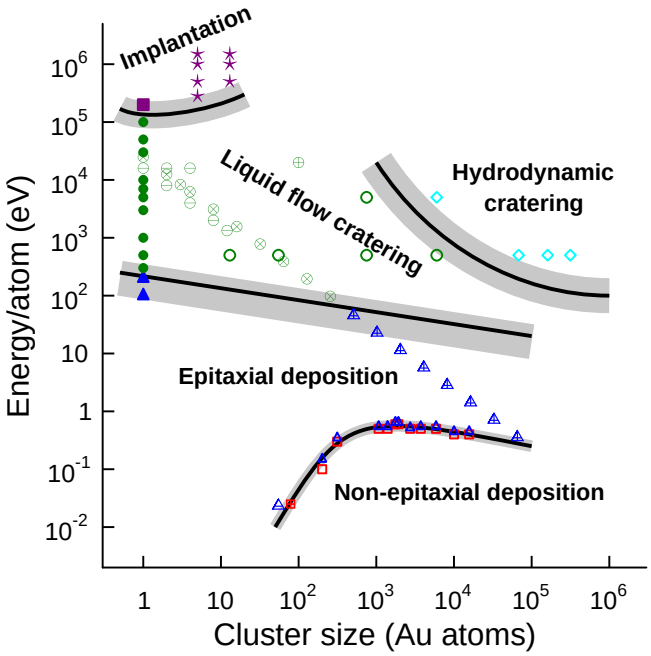

Figure 3: Phase diagram-like representation of the outcome of cluster deposition / impact events for gold particles deposited on gold. Each symbol represents an MD data point, see Ref. [18] for details and references. (Reprinted from Ref. [18] with kind permission from Springer. © Springer-Verlag 2008.)

typical meteorite impact velocities of around 22 km/s, the onset of macroscopic impact behaviour was found to occur around 50000 atoms, corresponding to particles of ∼12 nm in diameter [86].

5.2 Epitaxial vs. non-epitaxial deposition

The work in this thesis concentrates on the border between epitaxial and non-epitaxial deposition. In depositing cluster-assembled thin films, the film morphology is largely determined by two factors, the deposition energy and cluster size [17, 18, 87]. With high energy deposition, dense films with large grain sizes are obtained, whereas with lower energies, the films are porous. Whether the films are nanocrystalline or not depends on how the crystal lattices in the deposited particles align with each other upon deposition. For low energy deposition ($\lesssim 10^{-2}$ eV/at), epitaxial alignment and grain growth is not aided by the deposition energy and may be caused by several processes. These are the subject of publications **I** and **II**.

For very low energy deposition of relatively large (5–20 nm) particles, the formation of a contact epitaxial layer at the particle-substrate interface occurs, as shown for example for silver particles on copper [88]. This can be considered the minimum of epitaxial alignment and the resulting cluster-assembled film would be both porous and nanocrystalline. For smaller deposited particles, a different

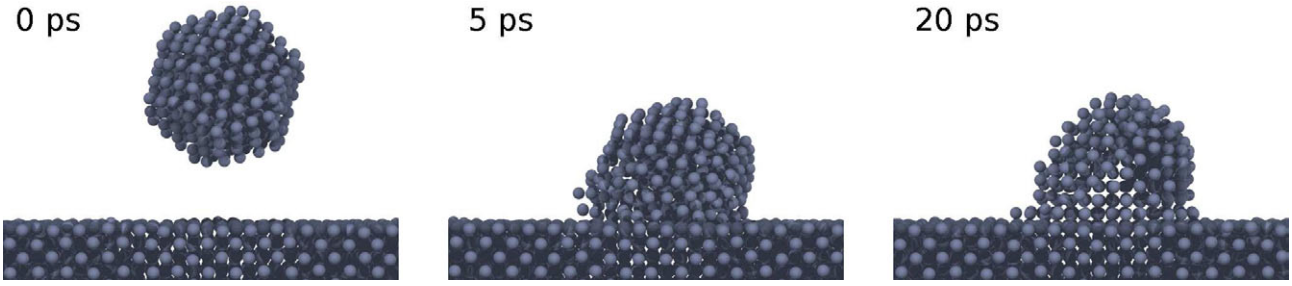

Figure 4: Snapshots of a typical low energy cluster deposition event. A metal cluster is deposited on a (100) surface. After the cluster has settled, large non-epitaxial regions remain in its upper part.

structure is typical. As the size of the contact epitaxial layer becomes comparable to the cluster radius, partial epitaxial alignment occurs and the non-epitaxial parts become accomodated to the rest of the particles by twin grain boundaries [89, 90]. This behaviour is typical to fcc metals, as their twin boundary energies are usually low. A typical configuration is illustrated in Fig. 4, where snapshots are shown of a typical deposition event.

It can be expected that at some point, with decreasing cluster size, fully epitaxial deposition occurs. The limiting case is clearly single atom deposition. This transition from epitaxial to non-epitaxial deposition (see Fig. 3) has been quantified for homoepitaxial deposition of metallic and alloyed clusters in Ref. [91] and in publications **I** and **II**. This was done for deposition energies low enough not to affect alignment. A linear relationship was discovered between deposition temperature and the radius of the largest cluster size able to align epitaxially upon deposition. The critical cluster sizes, above which non-epitaxial deposition dominates, are shown in Fig. 5(a) for alloyed metal clusters [**II**], and were found to be between 20 and 2000 atoms, depending on temperature. The results for elemental metals are similar [**I**].

5.3 Mechanical melting upon deposition

As a cluster lands on the surface, bonds form between the cluster and substrate atoms. For metals, the released energy is substantial, and can lead to the melting of small clusters [**I**]. However, the notion of melting upon deposition is not trivial. The interface formation between the cluster and substrate upon deposition takes place in time scales on the order of 10 ps, as shown for a 13 atom Cu_3Ni cluster in Fig. 5(b). In such a short time, the system will not have time to reach thermodynamic equilibrium and it is far from obvious whether melting, which is thermodynamically a nucleation-and-growth process, is relevant. There is, on the other hand, a melting process that does not require nucleation and growth. Mechanical, or superheated, melting occurs when the temperature is so high that the crystal lattice is no longer (meta)stable. The system then melts homogeneously. The temperature at which this

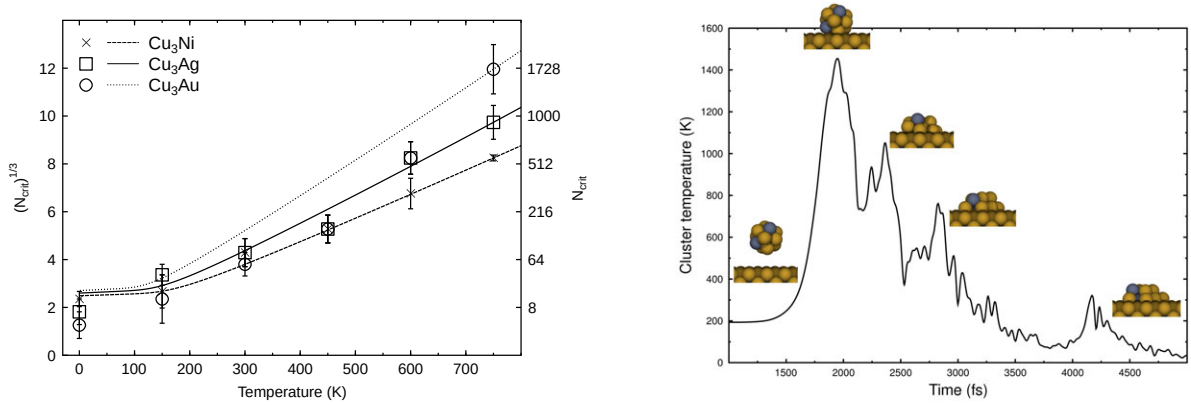

(a) (b)

Figure 5: (a) Critical cluster sizes above which non-epitaxial deposition occurs for low energy cluster deposition of nanoalloys. (b) Evolution of the temperature as a 13 atom Cu_3Ni cluster is deposited on $Cu_3Ni(100)$ at 0 K. (Both figures from publication **II**.)

happens is, for a wide range of materials, around 15–20 % higher than the thermodynamic melting point [92–94]. In publication **I**, the mechanical melting point was used as a measure of the stability of the crystal structure of a deposited cluster.

The cluster size dependence of the heating upon deposition can be obtained from simple physical arguments [**I**]. For a cluster that just melts upon deposition, the energy released from the cluster-surface bonds has to be equal to the energy required to heat it up to the melting temperature,

$$\frac{3}{2}Nk_B\Delta T = \frac{\Delta E}{2}, \tag{6}$$

where $\Delta T = T_{\mathrm{melt}} - T_i$ is the required heating, starting at the initial temperature T_i, and N the number of atoms in the cluster. The released surface energy is $\Delta E = \frac{2\gamma A}{\beta}$, where it's assumed that a surface energy γ is released from an area two times the area of a segment of a sphere with height h, so that $A = 2\pi rh$, where r is the cluster radius. The factor β illustrates the fraction of energy that goes into heating the cluster and is taken as $\beta = 2$, corresponding to half the energy to the cluster and half to the substrate.

Assuming that a molten cluster will recrystallize epitaxially, the above leads to an expression for the critical cluster size,

$$r_{\mathrm{crit}} = \sqrt{\frac{\gamma h a^3}{4k_B\beta}}\frac{1}{\sqrt{T_{\mathrm{melt}} - T_i}}. \tag{7}$$

where a is the lattice constant of the material. (This equation assumes that the material has the fcc crystal stucture, but a corresponding equation is easy to derive for any material.)

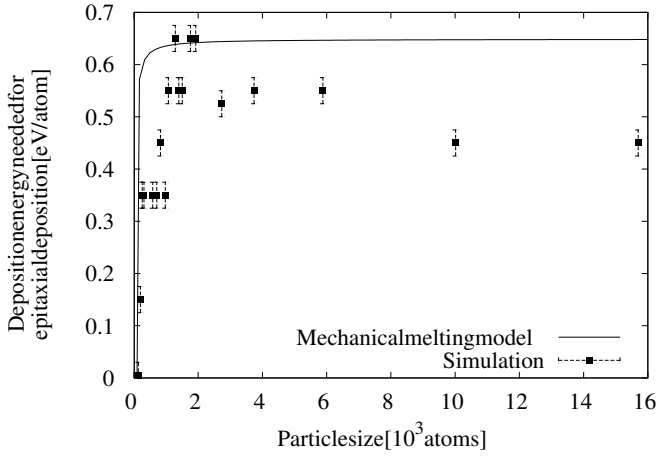

Figure 6: Energy needed for epitaxial deposition as a function of particle size. (Reprinted from Ref. [18] with kind permission from Springer. © Springer-Verlag 2008.)

Eq. (7) reproduces the low temperature limit of epitaxy in Fig. 5(a) very well. It is important to note that the model has no fitted parameters, only material properties are used.

The same model can also be used to describe more energetic particle deposition. To predict the energy required to epitaxially deposit nanoparticles up to thousands of atoms [17, 18], the deposition energy (E_k) can simply be added to the energy released due to interface formation, so that $\Delta E \rightarrow \Delta E + c\,E_k$, where c is an efficiency factor, which can be assumed to be $c = 0.5$, in analogy with β [18]. The resulting curve is compared to simulation data from Ref. [17] in Fig. 6. As particle size grows, the energy per atom needed for epitaxial deposition increases rapidly. As the size tends towards infinity, the model predicts that the energy saturates to a constant value. The simulation data show, however, that the energy goes down a little with particle size after reaching its maximum. The reason for this discrepancy lies in the fact that due to finite heat conductivity, very large particles remain at a higher temperature for a longer time, thus allowing them to align epitaxially more efficiently than smaller particles. Heat conductivity is ignored by the model, which thus predicts saturation instead of decline after the maximum.

5.4 Dislocation mechanism

The temperature dependence of the mechanical melting mechanism described in the previous section is far too weak to explain the fact that rather large particles align epitaxially at the highest temperatures (see Fig. 5(a)). The melting model alone would for example predict critical cluster sizes of $\lesssim$100 atoms at 750 K. Clues of the mechanisms by which epitaxiality is achieved without melting can, however, be obtained from the structures of the as-deposited particles around the critical size. They

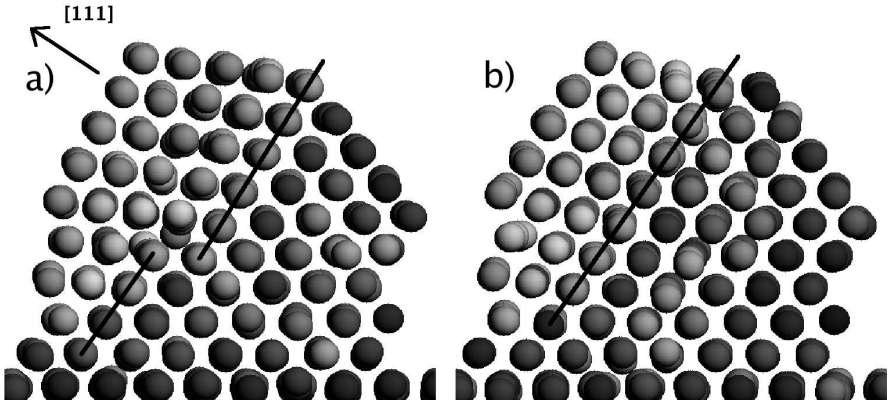

Figure 7: Typical configuration for a 405 atom cluster deposited at 450 K. In part (a), the twin boundary (indicated by a line) is kinked. In part (b), a dislocation has moved through the boundary, moving it by one atomic plane. In both parts, the non-epitaxial part of the cluster is to the upper left of the boundary. (From publication **I**.)

show that the non-epitaxial and epitaxial parts are separated by {111} twin boundaries [89, 90], as illustrated in Fig. 7. This is the natural configuration for fcc metals, as their twin boundary energies are low.

In publications **I** and **II**, it was shown that the twin boundaries can migrate via dislocation motion. A single event is shown in Fig. 7, where the non-epitaxial part of a deposited cluster gets diminished as the twin boundary moves by one atomic layer. The dislocations are thermally activated, leading to the observed fast increase of the critical size with temperature.

A model of the de-twinning was established in publication **I**. The migration barrier for a dislocation of length l, where l can be taken equal to the cluster diameter $2r$, is

$$E_{\text{activ}} = (\gamma_{UTB} - \gamma_{TB})\, b\, (2r), \tag{8}$$

where b is the distance moved by the dislocation. For twin boundaries, the dislocation is a Shockley partial dislocation, so $b = \frac{a}{\sqrt{6}}$, where a is the lattice constant [95]. The barrier $\gamma_{UTB} - \gamma_{TB}$ is the difference between the unstable and stable twinning fault positions [96].

If one assumes that the number of dislocations that have to be thermally activated to achieve epitaxy is $n = r/d_{\{111\}}$, where $d_{\{111\}}$ is the (111) layer distance, the following relation holds between the cluster size and activation energy [**I**],

$$n = \frac{r}{d_{\{111\}}} \propto t\, \nu_D\, r\, e^{-E_{\text{activ}}(N_{\text{crit}})/k_B T}, \tag{9}$$

where t is the simulation time (2 ns in publications **I** and **II**) and ν_D the Debye-frequency.

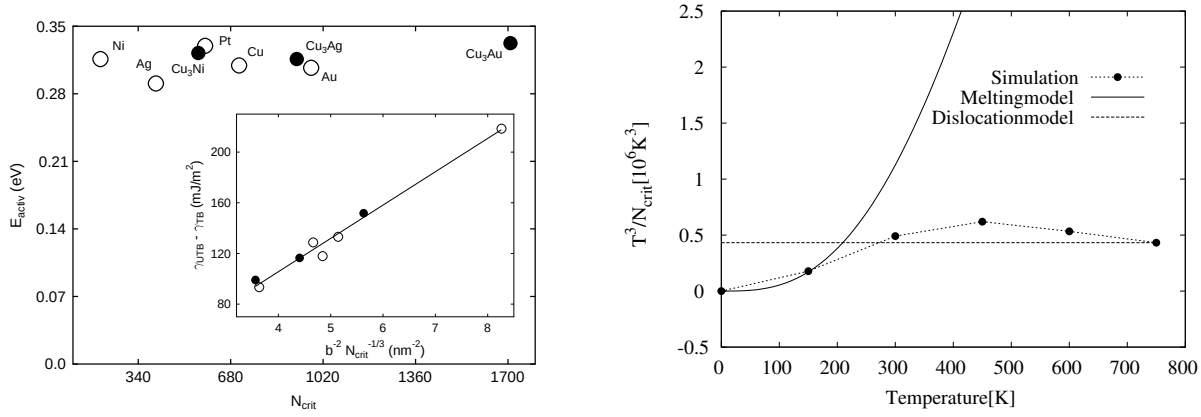

(a) (b)

Figure 8: (a) Activation energies for dislocation motion in clusters at the critical cluster size at 750 K. The inset shows the correlation between the critical size and the barrier $\gamma_{UTB} - \gamma_{TB}$. (b) Transition from mechanical melting to dislocation dominated epitaxial alignment for Au clusters deposited on Au. (From publications **I** and **II**.)

As the simulation time is constant,

$$e^{-E_{\text{activ}}(N_{\text{crit}})/k_B T} \propto \frac{1}{d_{\{111\}}\nu_D} \approx \text{const.} \tag{10}$$

for the critical cluster sizes N_{crit}. The factor $1/d_{\{111\}}\nu_D$ is constant within $\sim$20 % between the alloys studied in publication **II** and within $\sim$30 % between the elements in publication **I**.

Thus, the activation energy at the critical cluster size should be constant. Indeed, as shown in Fig. 8(a), it is ca. 0.3 eV for all the materials studied. The dislocation model can also explain the linear high-temperature dependence of the critical cluster size shown in Fig. 5(a). It follows from Eq. (10) that the fraction $\frac{E_{\text{activ}}}{T}$ is constant, and thus, from Eq. (8), $N_{\text{crit}}^{1/3} \propto T$.

The transition from mechanical melting to dislocation dominated epitaxial alignment is illustrated in Fig. 8(b) for deposition of gold clusters on gold. The transition happens at around 200-300 K for cluster sizes of ca. 50 atoms [**I**].

The two different models can be combined into a single expression by replacing r by $r - r_{\text{mm}}$ in Eq. 9, where r_{mm} is the critical cluster size as given by the melting model in Eq. 7 [**II**]. The resulting solution has the correct property that it gives larger critical cluster sizes than the individual mechanisms and reduces to them at the extremes.

The resulting curves are shown for alloyed clusters in Fig. 5(a) [**II**], and reproduce well the simulation data. Similar reproduction is found for elemental metal clusters [**I**]. Epitaxial alignment is thus

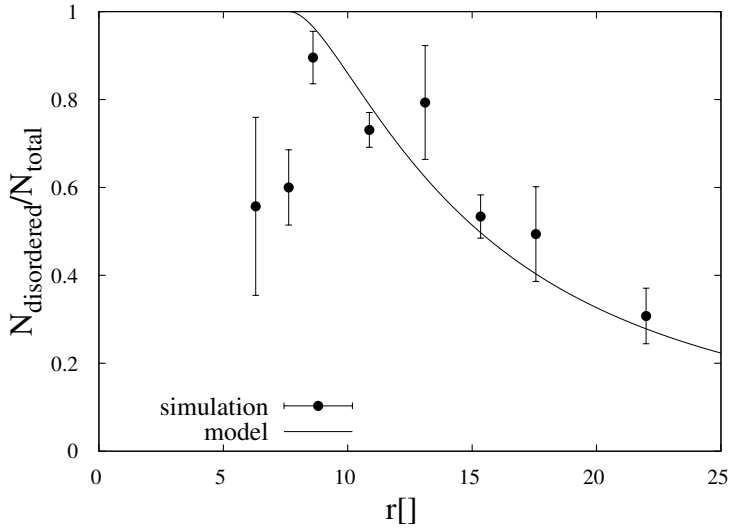

Figure 9: Fraction of the cluster chemically disordered upon low energy deposition. (From publication **II**.)

achieved by two physical processes, mechanical melting upon deposition, and thermally activated dislocation motion on longer time scales.

5.5 Alloy disordering upon deposition

Besides epitaxial reorientation, deposition induces chemical disordering in alloyed clusters [97]. It is shown in publication **II** that the mechanisms determining epitaxial alignment are the same for alloyed as for elemental clusters, and that whether the cluster is ordered or not does not significantly affect alignment. This was found to be the case for the alloys shown in Fig. 5(a), comparing the deposition of clusters in disordered and $L1_2$-ordered phases.

However, for ordered particles, deposition is found to lead to disordering [97]. In publication **II**, a systematic cluster size dependence for the extent of the disordering was established. The dependence turned out to be surprisingly simple. Assuming a spherical shape for the particles, a segment of $\sim$1.5 nm in contact with the substrate was disordered after deposition. The resulting curve for the disordered fraction as a function of particle size is shown in Fig. 9 and compared to simulation results. The spherical model loses its meaning for the two smallest cluster sizes in the figure, as the cluster diameter becomes smaller than the segment height, 1.5 nm. For all sizes above this limit, the correspondence is perfect.

This disordering behaviour explains the fact that ordering of the incoming particle doesn't affect epitaxial alignment. The cluster sizes that are able to align epitaxially are small enough so that they

are mostly disordered upon deposition.

5.6 Discussion

Understanding the deposition kinetics of individual clusters is a prerequisite to understanding thin film deposition by cluster ions. It has been shown that the same mechanisms of mechanical melting and dislocation motion determine epitaxial alignment for multiple cluster deposition [87, 98, 99]. However, especially the effect of the heating-induced mechanical melting is lessened by surface roughness, so that the critical cluster size is smaller for thin film deposition [98].

To fully predictively model thin film deposition, several other factors need to be taken into account. On longer time scales, in systems were wetting is favorable, surface diffusion will work towards reducing the clusters to a monolayer [100, 101]. In the case of alloyed clusters, the extent of segregation occurring between closeby cluster impacts is an open question. To fully model these, a scheme of alternating molecular dynamics and Monte Carlo (MC) simulations could be developed, with cluster deposition on short time scales being modelled by MD and segregation, surface diffusion, and possibly dislocation activity by MC. Such a scheme would allow the construction of a full phase diagram of cluster-assembled film structure as a function of cluster size, composition, deposition energy, and flux.

6 IRRADIATION EFFECTS IN NANOPARTICLES

Ion irradiation is a widely used method in the semiconductor industry for tuning material properties. It can be used, *e.g.*, for doping, controlling and smoothing surface features, and enhancing ordering in alloyed systems [11–15].

As many properties of nanostructures are different from those of the corresponding macroscopic material, the question arises how the response to ion irradiation is affected by the target size. While much effort has been put into understanding nanoparticle formation and structure modification by ion beams inside solid matrices [102], very little is known of the irradiation response of free or supported nanoparticles. These questions are addressed in publications **III–VI** for the cases of metal and metal alloy nanoparticle targets.

Ion impacts on different materials induce a wide range of phenomena [11, 12, 103–105]. For the purpose of this discussion, two main types of irradiation will be distinguished, namely irradiation with light and heavy ions. Light ions, such as helium, mainly produce point defects, such as vacancies

and interstitials, whereas heavier ions lead to collision cascades where the damage is more extensive. Also ionization can be expected as a result of irradiation [106]. Molecular dynamics cannot, however, be used to model charge effects.

The results below regarding irradiation effects in nanoparticles will be divided into three parts. First, damage production and defect formation by heavy and light ions will be discussed in sections 6.1.1 and 6.1.2. Irradiation-induced structural transformations are covered in section 6.2.

6.1 Damage production and sputtering

6.1.1 Sputtering by heavy ion irradiation

The response of gold nanoparticles upon 25 keV gallium irradiation was investigated in publication **III**. This type of irradiation is typical for secondary ion mass spectrometry (SIMS), for which it has been shown that vaporizing a metal layer or depositing metal nanoparticles on organic and polymeric substrates prior to SIMS analysis enhances the SIMS yields significantly and allows the detection of higher mass constituents [107–109].

To illustrate ion irradiation of nanoparticles, Fig. 10 shows snapshots of a typical irradiation event, where a massive ion hits a metallic nanoparticle. The impact causes several effects. In the beginning, lots of atoms are sputtered and most of the kinetic energy of the ion is transferred to the particle. The particle then thermalizes. The final temperature can well exceed the melting point [**V**]. Further, atoms may then be sputtered thermally from the high temperature particle [110]. Sometimes, when a suitable amount of energy gets deposited, the particle melts only partially [**V**].

Well-established theoretical tools exist for modelling linear cascade sputtering, such as that induced by 25 keV Ga impacting on Au [111]. The discussion below follows closely the treatment presented in publication **III**.

An irradiation event is illustrated in Fig. 11(b). An ion which impacts the target at $\mathbf{r}_0$ induces damage that is distributed according to an *a priori* unknown distribution F. The sputtering yield can be taken as proportional to the damage inflicted on the target surface ∂T, so that it is given by integrating the damage distribution over ∂T,

$$Y_0(\mathbf{r}_0) = \Lambda \int_{\partial T} \mathrm{d}^2\mathbf{r}\, F(\mathbf{r}, \mathbf{r}_0), \tag{11}$$

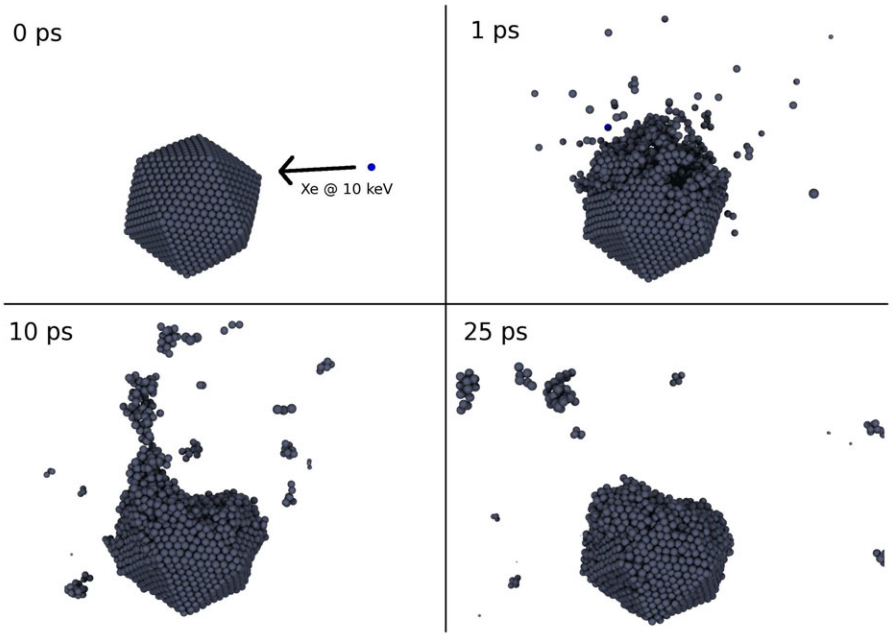

Figure 10: Snapshots of a 10 keV xenon ion impacting on a ∼4 nm platinum nanoparticle.

where Λ is a proportionality constant. The total sputtering yield is then given by the average of Eq. (11) over the ion impact point,

$$Y = \int \mathrm{d}^2\mathbf{r}_0 \, Y_0(\mathbf{r}_0) / \int \mathrm{d}^2\mathbf{r}_0. \tag{12}$$

It is often assumed that the damage distribution is not affected by the actual target surface [111]. Thus, before integrating over the surface, the distribution is assumed to be the same as it would be in an infinite bulk. In publication **III** the standard Gaussian distribution was used, so

$$F(\mathbf{r}, \mathbf{r}_0) = \frac{E}{(2\pi)^{\frac{3}{2}}\alpha\beta^2} e^{-\frac{1}{2\alpha^2}[z-z_0+a]^2} e^{-\frac{1}{2\beta^2}\left[(x-x_0)^2+(y-y_0)^2\right]}, \tag{13}$$

where E is the deposited energy, $\mathbf{r} = (x, y, z)$, and a gives the depth of the center of the distribution under the impact point $\mathbf{r}_0$.

Parametrizing the distribution can be done for example from binary collision simulations, as they are straightforward and computationally efficient [**III**]. For example the SRIM code [112] can be used for this purpose.

The proportionality constant can be obtained from the expression of the bulk sputtering yield [**III**],

$$Y_{\mathrm{bulk}} = \frac{2\pi\Lambda E}{(2\pi)^{\frac{3}{2}}\alpha} e^{-\frac{a^2}{2\alpha^2}}. \tag{14}$$

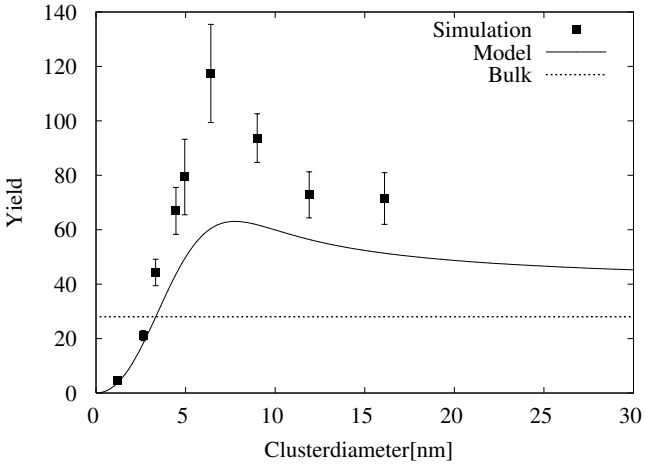

(a)

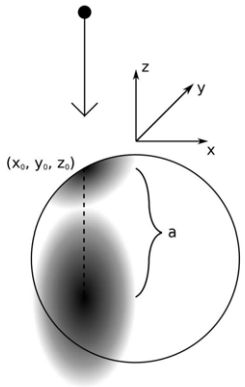

(b)

Figure 11: (a) Size-dependent sputtering yield of gold nanoparticles under 25 keV Ga bombardment. The horizontal line shows the bulk sputtering yield. (From publication **III**.) (b) Schematic of a cascade producing irradiation event in a nanoparticle. See text for further explanation. (Adapted from publication **III**.)

For a spherical nanoparticle of radius R, the yield is given by [**III**]

$$Y_{\text{particle}}(R) = 2\int_0^{\frac{\pi}{2}} \mathrm{d}\Theta_0 \cos\Theta_0 \sin\Theta_0 Y_0(R,\Theta_0), \tag{15}$$

where

$$Y_0(R,\Theta_0) = \frac{2\pi\Lambda E}{(2\pi)^{\frac{3}{2}}\alpha\beta^2} R^2 \int_0^{\pi} \mathrm{d}\Theta \sin\Theta I_0\left(\frac{R^2}{\beta^2}\sin\Theta\sin\Theta_0\right) \times e^{-\frac{R^2}{2\alpha^2}\left[\cos\Theta-\cos\Theta_0+\frac{a}{R}\right]^2-\frac{R^2}{2\beta^2}\left[\sin^2\Theta+\sin^2\Theta_0\right]}, \tag{16}$$

where Θ_0 is the polar angle of the ion impact point in spherical coordinates and I_0 is a modified Bessel function [113].

The resulting nanoparticle size dependence for the sputtering yield is shown in Fig. 11(a). While the yield is not reproduced quantitatively, the qualitative features agree with the simulations. The same method can also be used to model sputtering from thin films, for which the predictions are also quantitatively more accurate [**III**].

Note, however, that for nanoparticles the choice of the damage distribution function becomes crucial. The above model was used in Ref. [114] for 200 keV Ar irradiation of gold nanoparticles on sapphire (Al_2O_3). With the Gaussian damage distribution parametrized from a SRIM calculation, the sputtering yield predicted by the model was shown to be roughly two orders of magnitude lower than the experimental yield. The center of the damage was, however, inside the substrate well below the entire

nanoparticle. Thus, it is questionable whether the Gaussian form can be used at all for this case, as only the tail of the Gaussian overlaps with the nanoparticle surface over which the integral is taken. This leads to large errors, because the distribution is most accurately reproduced near the center of the Gaussian.

In fact, assuming that the 200 keV ion does not lose much energy while going through the particle, one can make the approximation that the energy deposited in the particle is given by the nuclear stopping multiplied by the distance traversed, $E = d_E\, h$. SRIM gives a value of $d_E = 84\,\mathrm{eV/Å}$ for 200 keV Ar in Au and, given for example a hemispherical shape for the particle, with radius R and radial coordinate r, h is given by $\sqrt{R^2 - r^2}$. As a zeroth order approximation, one can assume that all the energy is uniformly spread in the particle, so that the damage distribution is constant, $F = \frac{E}{V}$. Note that this approach differs somewhat from that used with the Gaussian distribution as both the deposited energy and the damage distribution are assumed to depend on particle size.

The sputtering yield for an ion impact at $\mathbf{r}_0$ is thus

$$Y_0(\mathbf{r}_0) = \Lambda \int_{\partial T} d^2\mathbf{r}\, F = \frac{3\Lambda E}{R}, \tag{17}$$

taking only the vacuum-facing part in the integral over ∂T, as it can be assumed that the interface towards the substrate would strongly hinder sputtering. Also gold sputtered on the sapphire surface can be expected to diffuse back to the clusters. Note that in this case, Y_0 is independent of the impact point, as the damage was assumed to be distributed uniformly in the particle. This is a reasonable approximation as the lateral dimensions of the cascade are comparable in size to the particle diameter. From the above equation

$$Y = \frac{1}{\pi R^2} \int d^2\mathbf{r}_0\, Y_0(\mathbf{r}_0) = 2\Lambda d_E. \tag{18}$$

The sputtering yield thus surprisingly turns out to be constant with respect to particle size. This can roughly be understood by the fact that the deposited energy per volume scales as R^{-2} while the surface area of the particle scales as R^2.

The constant yield is actually in this case in agreement with the experiments [114]. The experiments indicate that when the gold particles burrow into the substrate upon irradiation, size-dependent sputtering describes the results better. On the sapphire substrate, however, no burrowing occurs, and in that case also a constant sputtering yield fits the data.

More precise experiments are needed to determine the dependence of radiation damage on particle size, to validate or disprove results obtained from simulations and models. In any case, it is clear

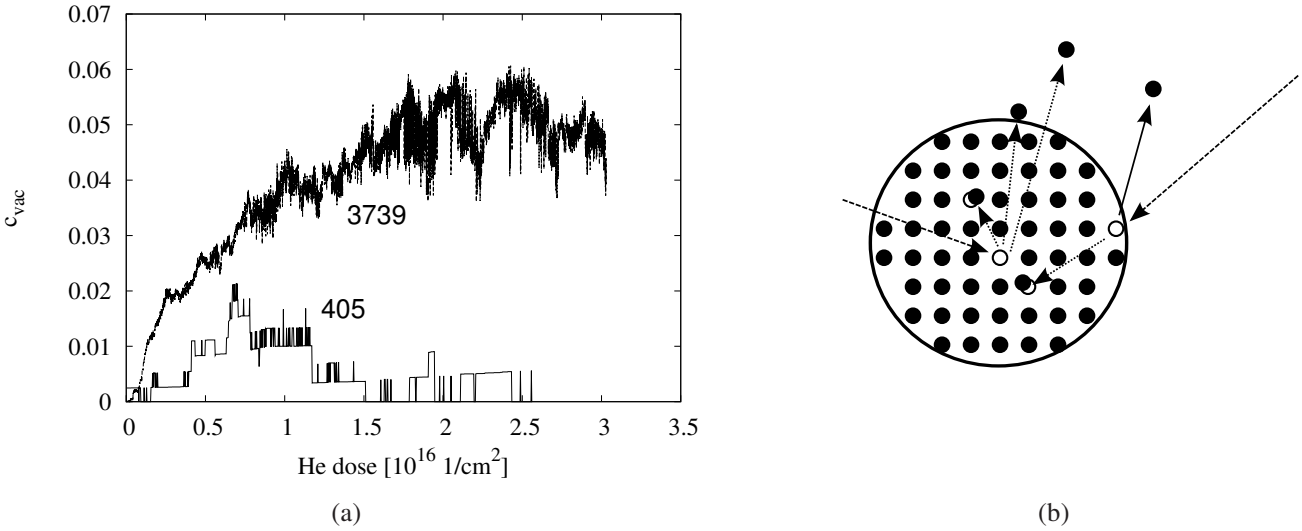

Figure 12: (a) Vacancy concentrations as a function of helium dose for nanoparticles of different sizes irradiated with 3 keV He. (b) Schematic of the processes induced in a nanoparticle by single knock-on irradiation events where no collision cascades are formed. (Both figures adapted from publication **IV**.)

that the choice of a realistic damage distribution function is a critical factor when models of the above kind are used for predictions. Also, automatic corrections for the damage distribution could be incorporated to improve quantitative correspondence [111].

6.1.2 Damage production by light ion irradiation

Light ion irradiation is characterized by a low scattering cross-section between the ion and target atoms. Thus collision cascades do not form and the irradiation is well described by binary collisions. In bulk, light ion irradiation mainly produces Frenkel pairs, and of course doping by the ion species. In a nanoparticle, there are several differences to this typical behaviour, mostly due to the always close-by surfaces.

First, the range of light ions in the target is usually much longer than the size of a nanoparticle, leading to significantly reduced doping, except for very low ion energies. The result of Frenkel pair production by irradiation is also different in a nanoparticle. Because the interstitial component of the pair usually travels significant distances ballistically, it often escapes the particle contributing to sputtering. If not, it will quickly diffuse to the particle surface, as the activation energy of interstitial migration is very low in most metals ($\sim$60 meV in Pt) [115]. This allows for a supersaturation of vacancies compared to bulk systems, as shown for 3 keV He irradiation of Pt nanoparticles of different sizes in publication **IV**. The processes occurring under light ion irradiation in the case of nanoparticles are illustrated in Fig. 12(b).

Fig. 12(a) shows the evolution of vacancy concentration with irradiation dose for Pt particles of 405 and 3739 atoms (ca. 2 and 5 nm in diameter), upon 3 keV He bombardment. In the smaller particle, the attained concentration is lower because vacancy clusters that become in contact with the particle surface are interpreted as surface roughness. For the larger particle, a concentration is attained that is higher than that in bulk, for which 4.3 % was obtained. This demonstrates the effect of the escaping interstitials. The maximum vacancy concentration achievable by irradiation, for the particle sizes studied in publication **IV**, is an increasing function of size. Unfortunately, high-dose irradiation simulations are extremely time-consuming and larger particle sizes could not be studied to determine the size at which the maximum vacancy concentration begins to decline towards the bulk value. Supposedly this will happen once the nanoparticle radius significantly exceeds the range of the ballistic interstitials.

A model based on kinetic equations for the number of atoms and vacancies was developed in publication **IV**. The processes shown in Fig. 12(b) were taken into account in the model and it was shown that the particles' irradiation response could be reproduced reasonably well. The model will be briefly reviewed here, the details being available in publication **IV**.

The model consists of the following two equations for the number of atoms (n_{at}) and vacancies (n_{vac}):

$$\begin{aligned} \frac{\mathrm{d}n_{\mathrm{vac}}}{\mathrm{d}n_{\mathrm{i}}} &= Y_d f(1-P_R) - \left(-\frac{\mathrm{d}n_{\mathrm{at}}}{\mathrm{d}n_{\mathrm{i}}}V_{\mathrm{at}}\right)\frac{n_{\mathrm{vac}}}{n_{\mathrm{at}}V_{\mathrm{at}}} - Y_{ds}(1-f)f_\Theta P_R, \\ \frac{\mathrm{d}n_{\mathrm{at}}}{\mathrm{d}n_{\mathrm{i}}} &= -Y_d f(1-P_R) - Y_{ds}(1-f)(1-f_\Theta P_R). \end{aligned} \tag{19}$$

n_{i} is the number of impacting ions. Introducing the model term by term, the first term in the upper equation gives the number of bulk vacancies created per impacting ion. The number of sputtered atoms, Y_d, from the Kinchin-Pease relation [116, 117] is modified by the fraction of bulk atoms (f) and the probability (P_R) that an interstitial will recombine with an already existing vacancy before leaving the particle. The second term gives the loss of vacancies due to the shrinking of the particle, given by the disappearing volume per impacting ion times the vacancy concentration. The last term is the contribution of recoiled surface atoms to vacancy recombination. The second equation gives the number of sputtered bulk and surface atoms.

The above model reproduces the simulation results in publication **IV** reasonably well, although the ion fluence at which the maximal vacancy concentration is obtained is somewhat overestimated. This is partly due to sub-threshold events, *i.e.*, events where not enough energy for sputtering is transferred. Such events are ignored by the model.

Unfortunately, while the model predicts increasing maximal vacancy concentrations with increasing particle size, it cannot be used to predict the size after which the concentration again starts declining towards the bulk value. Indeed, one of the most interesting questions is how high vacancy concentrations it is possible to obtain in nanoparticles under irradiation, at a theoretical maximum. For the larger particle in Fig. 12(a), which is around 5 nm in diameter, a concentration of about 6 % is achievable with 3 keV He ions, as shown above. In publication **IV**, also another scheme was employed. Random Pt atoms in the particle were given a kinetic energy of 100 eV directly, in a random direction. This method allows much faster simulations, as the high velocity ion can be omitted. Vacancy concentrations as high as $\sim$10 % were obtained. Although the method doesn't correspond directly to experimental conditions, the result gives an idea of what kind of concentrations it may be possible to achieve by carefully choosing irradiation parameters.

6.2 Structural transformations

The capability of ion beams to induce structural transformations in materials is one of their most useful features [12]. For instance, to achieve better magnetic properties, chemical ordering can be induced in thin films by a combination of ion irradiation and annealing, as already discovered by Néel *et al.* in the sixties [118, 119]. The role of irradiation in the process is to create point defects, the migration of which causes ordering. Ordering can in some cases be obtained even without annealing, making use of direct heating by the ion beam [14], but usually ion beams as such are associated with disordering, as they displace atoms from their lattice positions without regard to ordering.

Another example of a solid-solid phase transformation induced by ions is the diamond-graphite [120] transition in carbon [120]. Many materials are also amorphizable under irradiation [12, 121, 122].

The same structural transformations may of course also occur in nanoparticles, examples of which are the graphitization of diamond nanoparticles and the hcp-fcc transition in embedded Co particles [123, 124]. Also chemical ordering in, *e.g.*, FePt particles can be achieved by irradiation and annealing [125–128]. However, an important difference to bulk materials is that the ordering temperature depends on particle size, although not strongly [70, 129, 130]. For very small particles, the formation of a less well ordered shell region may additionally limit the overall ordering [70, 131].

Ordering can be promoted using light ion irradiation, usually helium at energies of a few keV [127]. Recently, this type of irradiation was also found to lead to a phase transformation where multiply twinned particles turned single-crystalline. The effect, which has so far been observed for FePt [132] and CuAu [**VI**], will be discussed in detail in the next section.

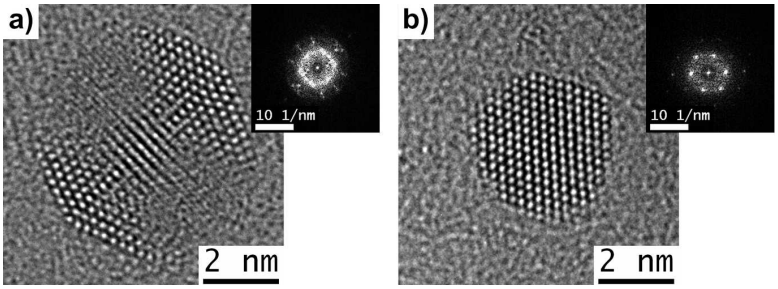

Figure 13: Typical CuAu nanoparticle structures (a) before and (b) after 0.5 keV helium irradiation. (From publication **VI**.)

Nanoparticles can support co-existing solid and liquid phases [31, 133]. It was shown in publication **V** that ion irradiation can lead to such configurations and that they in turn can lead to phase transformations. For a partly molten particle of multiply twinned icosahedral structure, the solid part underwent a transition to single crystallinity. The transformation occurred via an oscillation, *i.e.*, growing and diminishing, in the size of the melt, during which the solid crystal reorganized into single crystalline structure.

6.2.1 Multiply twinned to single-crystalline transition

Often when nanoparticles are produced in the gas phase, they form due to kinetic effects in structures that are not the global free energy minimum [25]. Such an effect is seen for example for FePt, for which multiply twinned particles form under certain conditions, although single-crystalline particles would be the ground state [134].

Upon helium irradiation with keV energies, it was recently discovered that such multiply twinned FePt particles could be turned single-crystalline [132]. The effect was later confirmed for CuAu [**VI**]. In both cases, the particles were created in the gas-phase and deposited onto amorphous carbon coated grids in ultra-high vacuum [134]. Fig. 13 shows transmission electron microscope (TEM) images of CuAu particles before and after 0.5 keV helium irradiation [**VI**]. Before irradiation, the particles are $\sim$5.6 nm in diameter and most ($\sim$60 %) are multiply twinned icosahedra. After irradiation, the grain boundary content in the particles has decreased dramatically, with $\sim$60 % of the particles being single-crystalline, up from $\sim$2 %. Also, the particle size is reduced because of sputtering, the mean diameter after irradiation being $\sim$3.3 nm. The ion fluence used in the experiment was rather high, $3 \cdot 10^{17}$ ions/cm^2 [**VI**].

This kind of a transformation is rather surprising because, as discussed in section 6.1.2, light ion irradiation is expected to produce point defects, mainly vacancies, in the particles, and these should not affect the stability of twin boundaries. Indeed, the response of an elemental Pt multiply twinned

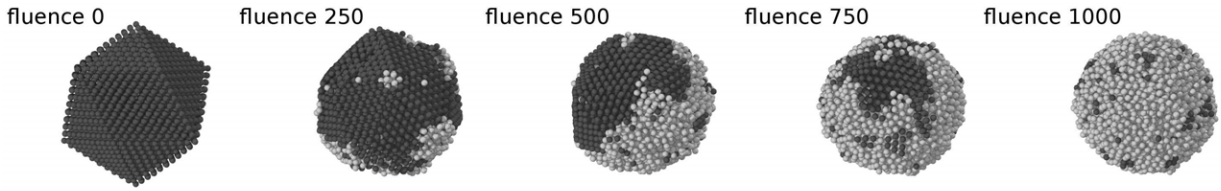

Figure 14: Structure of a ∼4 nm CuAu particle under 3 keV helium irradiation as a function of fluence. Light regions are amorphous and dark ones crystalline.

nanoparticle to high-fluence irradiation was investigated by molecular dynamics simulations in publication **V**, and no change in the grain boundary content was found. Pt was chosen as a model system since its grain boundary energy is very high, maximizing the driving force for a transition towards the single-crystalline state.

Perhaps even more surprisingly, similar high-fluence irradiation of CuAu and FePt nanoparticles leads to amorphization of the particles, as discovered by simulation in publication **VI**. Fig. 14 shows the change in the structure of a CuAu particle of about 4000 atoms upon 3 keV helium irradiation. The atoms are coloured according to the structure of their environment, as determined by an analysis based on bond correlation [79], so that amorphous and crystalline regions are distinghuished.

Amorphization of the CuAu nanoparticles is surprising as the alloy is not known to amorphize under irradiation in bulk [135, 136]. The same applies for FePt [14, 137, 138], but FePt nanoparticles also amorphize in the simulations [**VI**]. Nonetheless, the simulations in publication **VI** are not in conflict with experiments. Fig. 15(a) shows how the fraction of crystalline atoms evolves in nanoparticles and in bulk. In the case of Fig. 15(a), damage is produced by initiating 300 eV cascades by giving the energy directly to a metal atom, similarly to the approach used for Pt particles in publication **IV** and discussed above, in Sect. 6.1.2. Although simplified, the method retains the qualitative amorphization behaviour. From the figure, it is clear that no amorphization occurs in bulk, in agreement with experiments. The same was found to be the case for a bulk surface [**VI**].

In the experiments of Ref. [132] and publication **VI**, no amorphous particles are observed in the TEM. This apparent discrepancy between the experiments and simulations is explained by the fact that no macroscopic times can be simulated with molecular dynamics. Thus recrystallization effects are ignored by the simulations. Recrystallization is a thermally activated process that can be assumed to have a low barrier in both CuAu and FePt, as otherwise the alloys could have been amorphized also in bulk in earlier experiments [14, 135–138]. Because of the non-amorphizability, no experimental values for the recrystallization activation energies exist. A very low value of around 60 meV was found for CuAu by simulation in publication **VI**, but the uncertainty of the number is quite high, as the amorphous phase has obviously not been considered in fitting the interatomic potential.

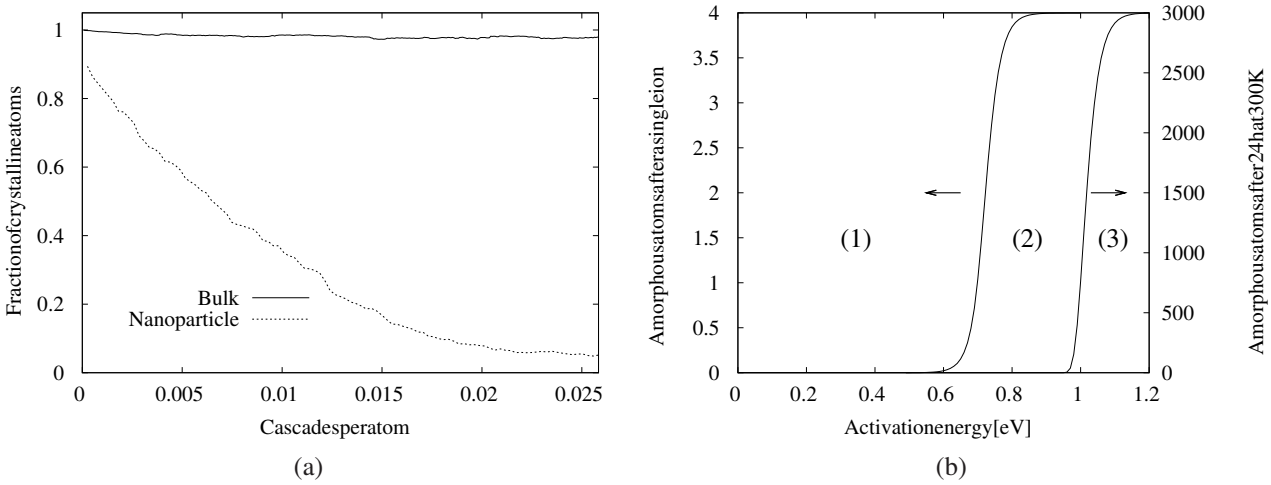

Figure 15: (a) Fraction of crystalline atoms in a ∼4000 atom CuAu nanoparticle and bulk CuAu as a function of the number of 300 eV cascades per atom. (Adapted from publication **VI**.) (b) Three regimes of behaviour under amorphizing irradiation, depending on the recrystallization activation energy: (1) transient partial amorphization, (2) complete amorphization + recrystallization, (3) stable amorphous phase at room temperature. See text for details.

Bounds for the activation energy, as obtained in publication **VI**, are shown in Fig. 15(b). The left curve in the figure was obtained by considering the time scale required to recrystallize a partially amorphized particle after a single ion impact. For activation energies smaller than this, the amorphization is transient. The right curve represents the number of amorphous atoms left in a completely amorphized particle after 24 hours. For activation energies higher than those shown by the curve, the amorphous particles will be stable at room temperature and should thus be visible in the TEM. In the middle is a regime where the particles would be completely amorphized by the irradiation but would recrystallize before TEM analysis.

Both experiments [14, 135–138] and the low activation energy found by simulation (see above) suggest that transient amorphization is the correct scenario. Transient amorphization thus leads to the multiply twinned to single-crystalline transformation in nanoparticles. The single-crystalline phase is favored in two respects in the process. First, multiply twinned particles amorphize over a factor of two faster than single-crystalline ones [**VI**], as amorphization is pronounced near grain boundaries [139]. Second, the recrystallization favours crystallization to the ground state phase, *i.e.*, towards single-crystallinity.

In conclusion, the tranformation pathway from multiply twinned to single-crystalline nanoparticles proposed in publication **VI** is illustrated schematically in Fig. 16.

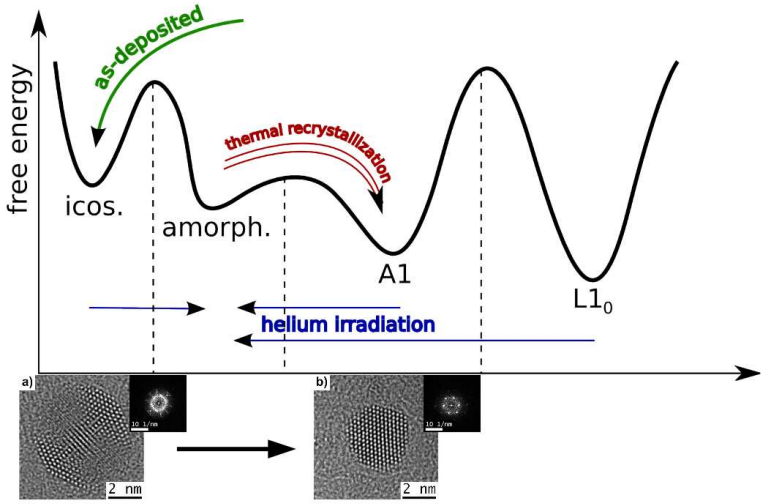

Figure 16: Schematic of the transition pathway from as-deposited multiply twinned (icosahedral) to single-crystalline (A1) particles. Helium irradiation causes amorphization and the amorphous phase thermally recrystallizes. Two effects favour the single-crystalline phase. First, amorphization of the twinned structures is more efficient. Second, it is favorable to recrystallize to the lowest energy structure. (Adapted from publication **VI**.)

6.2.2 Discussion

In general, many bimetallic alloys are known to amorphize readily [121]. No widely accepted theory exists, however, to predict whether a certain alloy will amorphize under given irradiation conditions or not. The result obtained in publication **VI**, that nanoparticles can be amorphized by irradiation while the corresponding bulk alloy cannot, is supported by recent literature. For instance, it has been demonstrated that while zirconia is very resistent to amorphization in bulk, in nanocrystalline form it can be amorphized quite easily [140]. Also Si and Ge nanocrystals embedded in silica have been shown to amorphize more easily with decreasing particle size [141]. There are even results that suggest that embedded copper particles could be amorphized by irradiation, but in the case of embedded particles, mixing with the substrate is always a concern [142]. Thus, the results in publication **VI** show for the first time that free or supported nanoparticles can be amorphized while the corresponding bulk alloy cannot.

The very special pathway of the twinned to single-crystalline transformation also provides an excellent experimental test for the transient amorphization. Since elemental metal nanoparticles should not amorphize, they also should not exhibit the de-twinning transition. It was indeed shown in publication **V** that elemental Pt nanoparticles do not undergo any transformation upon light ion irradiation. Thus investigating the response of elemental nanoparticles to irradiation should reveal whether, first, the transformation exists in them, and second, if it is similar to the one in alloyed particles.

Another intriguing possibility suggested by the result in publication **VI** is that the amorphous CuAu and FePt nanoparticles should be directly observable. In a setup where ion irradiation could be carried out at low temperature, the amorphous phase should be stable as recrystallization would be inhibited. The amorphous state could then be observed either *in situ*, or, keeping the temperature low during transport, after irradiation.

7 CONCLUSIONS

In this thesis, two mechanisms were found to contribute to epitaxial alignment of clusters deposited from the gas phase, mechanical melting upon deposition and dislocation motion on longer time scales. An understanding of these mechanisms paves way for choosing optimal conditions for low energy cluster deposition, allowing the desired cluster film structures to be achieved. The mechanisms identified for metal clusters are also sufficiently general that they may be directly transferable to, for example, semiconductor materials, but further study is required to establish whether this is the case.

Size-dependencies of damage production upon ion irradiation are basic knowledge that allows experimental results to be understood and analyzed. The models developed in publications **III** and **IV** allow an understanding of processes where nanoparticles are subjected to irradiation.

The multiply twinned to single-crystalline transition in nanoparticles under light ion irradiation gives a new tool to control nanoparticle structure. From the point of view of basic science, the amorphization found in publication **VI** for the two bimetallic alloys that do not amorphize in bulk is of primary interest. This is the first time enhanced amorphization is found for supported nanoparticles, neither embedded in a matrix nor part of a cluster-assembled or nanocrystalline film.

Experimental evidence of the amorphization is so far indirect and based on the observed twinned to single-crystalline transformation. At least two kinds of experiments can be made to test the prediction. Irradiation of elemental metal particles should not lead to amorphization and transformation, or at least the mechanism should be very different. Another possibility is to irradiate alloyed particles *in situ* in a TEM, at low temperature to prevent recrystallization, to observe the amorphous particles directly.

The precise control of nanoparticle properties is of primary importance for designing materials for specific applications. Ion irradiation is turning out as a valuable tool for obtaining nanoparticles in unexpected phases, and provides a multitude of possibilities for exploring basic physics in well-controlled systems. This thesis constitutes a significant part of the research on radiation effects in nanoparticles, as previous results especially on free or supported particles are scarce.

ACKNOWLEDGMENTS

I wish to thank the head of the Department of Physics, Prof. Juhani Keinonen, as well as the head of the Accelerator Laboratory, Prof. Jyrki Räisänen, for providing the facilities for conducting the research presented in this thesis.

The greatest of thanks are due to my supervisor, Prof. Kai Nordlund. Your optimistic attitude towards physics and the life of a scientist in general have made working with you both enjoyable and productive. I am equally grateful to my long-standing collaborator, Prof. Karsten Albe from the Technische Universität Darmstadt. Your rigorous approach to science has taught me a lot, and working with you has been a pleasure. Many thanks are also due to Dr. Antti Kuronen. Your door has always been open, and I've enjoyed these years of working together.

Thanks are due to all my collaborators, especially Dr. Bernd Rellinghaus and Darius Pohl from IFW Dresden, whose beautiful experiments are the reason I began studying irradiation of nanoparticles in the first place.

I am dearly indebted to all my colleagues, friends, at the laboratory and department. The endless coffee breaks spent talking about science and (mostly) everything else have made these years unforgettable. Special thanks are due to Sami, Toffe, Caro, Jani, Nicke and Eero. I also want to thank all my Swedish-speaking colleagues for their encouragement in improving my language.

Many thanks are due to all my friends, relatives, and especially my family. I would not be here without you.

Finally, the most important thanks are due to my wife Paula. You have been amazingly encouraging and patient, and you balance my life between working and the important things in life.

Financial support from the Magnus Ehrnrooth Foundation and the Vilho, Yrjö and Kalle Väisälä Fund are gratefully acknowledged.

Freiburg, October 8th, 2009
Tommi Järvi

References

1. P. Pawlow, *The dependence of the melting point on the surface energy of a solid body*, Z. Phys. Chem. **65**, 1 (1909).

2. I. Freestone, N. Meeks, M. Sax, and C. Higgitt, *The Lycurgus Cup — A Roman Nanotechnology*, Gold Bulletin **40**, 270 (2007).

3. M. Reibold, P. Paufler, A. A. Levin, W. Kochmann, N. Pätzke, and D. C. Meyer, *Carbon nanotubes in an ancient Damascus sabre*, Nature **444**, 286 (2006).

4. K. W. Urban, *Is science prepared for atomic-resolution electron microscopy?*, Nature Materials **8**, 260 (2009).

5. W. Xu, J. S. Kong, Y.-T. E. Yeh, and P. Chen, *Single-molecule nanocatalysis reveals heterogeneous reaction pathways and catalytic dynamics*, Nature Materials **7**, 992 (2008).

6. F. Schäffel, C. Kramberger, M. H. Rümmeli, R. Kaltofen, D. Grimm, A. Grüneis, E. Mohn, T. Gemming, T. Pichler, B. Büchner, B. Rellinghaus, and L. Schultz, *Carbon nanotubes grown from individual gas phase prepared iron catalyst particles*, Phys. Status Solidi A **204**, 1786 (2007).

7. M. J. Biercuk, M. C. Llaguno, M. Radosavljevic, J. K. Hyun, and A. T. Johnson, *Carbon nanotube composites for thermal management*, Appl. Phys. Lett. **80**, 2767 (2002).

8. P. Melinon, V. Paillard, V. Dupuis, A. Perez, P. Jensen, A. Hoareau, J. P. Perez, J. Tuaillon, M. Broyer, J. L. Vialle, M. Pellarin, B. Baguenard, and J. Lerme, *From free clusters to cluster-assembled materials*, Int. J. Mod. Phys. B **9**, 339 (1995).

9. R. Narayanan and M. A. El-Sayed, *Shape-Dependent Catalytic Activity of Platinum Nanoparticles in Colloidal Solution*, Nano Lett. **4**, 1343 (2004).

10. Y. Tang and M. Ouyang, *Tailoring properties and functionalities of metal nanoparticles through crystallinity engineering*, Nature Materials **6**, 754 (2007).

11. *Sputtering by Particle Bombardment I*, Vol. 47 of *Topics in Applied Physics*, edited by R. Behrisch (Springer-Verlag, Berlin, 1981).

12. M. Nastasi and J. W. Mayer, *Thermodynamics and kinetics of phase transformations induced by ion irradiation*, Mat. Sci. Rep. **6**, 3 (1991).

13. M. Joe, C. Choi, B. Kahng, and J.-S. Kim, *Nanopatterning by dual-ion-beam sputtering*, Appl. Phys. Lett. **91**, 233115 (2007).

14. C.-H. Lai, C.-H. Yang, and C. C. Chiang, *Ion-irradiation-induced direct ordering of $L1_0$ FePt phase*, Appl. Phys. Lett. **83**, 4550 (2003).

15. F. Frost, R. Fechner, B. Ziberi, J. Völlner, D. Flamm, and A. Schindler, *Large area smoothing of surfaces by ion bombardment: fundamentals and applications*, J. Phys.: Condens. Matter **21**, 224026 (2009).

16. E. Salonen, T. Järvi, K. Nordlund, and J. Keinonen, *Effects of the surface structure and cluster bombardment on the self–sputtering of molybdenum*, J. Phys. Condens. Matt. **15**, 5845 (2003).

17. K. Meinander, K. Nordlund, and J. Keinonen, *Size dependent epitaxial cluster deposition: The effect of deposition energy*, Nucl. Instrum. Methods Phys. Res. B **242**, 161 (2006).

18. K. Nordlund, T. T. Järvi, K. Meinander, and J. Samela, *Cluster ion-solid interactions from meV to MeV energies*, Appl. Phys. A **91**, 561 (2008).

19. T. T. Järvi, A. Kuronen, M. Hakala, K. Nordlund, A. C. T. van Duin, W. A. Goddard III, and T. Jacob, *Development of a ReaxFF description for gold*, Eur. Phys. J. B **66**, 75 (2008).

20. M. Brust, M. Walker, D. Bethell, D. J. Schiffrin, and R. Whyman, *Synthesis of thiol-derivatized gold nanoparticles in a 2-phase liquid-liquid system*, J. Chem. Soc., Chem. Commun. 801 (1994).

21. F. Ren, X. H. Xiao, G. X. Cai, J. B. Wang, and C. Z. Jiang, *Engineering embedded metal nanoparticles with ion beam technology*, Appl. Phys. A **96**, 317 (2009).

22. M. G. del Muro, Z. Konstantinovic, M. Varela, X. Batlle, and A. Labarta, *Metallic Nanoparticles Embedded in a Dielectric Matrix: Growth Mechanisms and Percolation*, J. Nanomater. 475168 (2008).

23. G. Wulff, *Zur Frage der Geschwindigkeit des Wachstums und der Auflösung der Krystallflachen*, Zeitschr. Krystallogr. Mineral. **34**, 449 (1901).

24. R. Dobrushin, R. Kotecký, and S. Shlosman, *Wulff Construction: A Global Shape from Local Interaction*, Vol. 104 of *Translations of Mathematical Monographs* (American Mathematical Society, Providence, USA, 1992).

25. F. Baletto and R. Ferrando, *Structural properties of nanoclusters: Energetic, thermodynamic, and kinetic effects*, Rev. Mod. Phys. **77**, 371 (2005).

26. M. Müller and K. Albe, *Structural stability of multiply twinned FePt nanoparticles*, Acta Mater. **55**, 6617 (2007).

27. M. Brack, *The physics of simple metal clusters: self-consistent jellium model and semiclassical approaches*, Rev. Mod. Phys. **65**, 677 (1993).

28. W. A. de Heer, *The physics of simple metal clusters: experimental aspects and simple models*, Rev. Mod. Phys. **65**, (1993).

29. B. Cao, A. K. Starace, C. M. Neal, M. F. Jarrold, S. Núñez, J. M. López, and A. Aguado, *Substituting a copper atom modifies the melting of aluminum clusters*, J. Chem. Phys. **129**, 124709 (2008).

30. K. Koga, T. Ikeshoji, and K. Sugawara, *Size- and Temperature-Dependent Structural Transitions in Gold Nanoparticles*, Phys. Rev. Lett. **92**, 115507 (2004).

31. D. Schebarchov and S. C. Hendy, *Static, transient, and dynamic phase coexistence in metal nanoclusters*, J. Chem. Phys. **123**, 104701 (2005).

32. C. B. Murray, D. J. Norris, and M. G. Bawendi, *Synthesis and Characterization of Nearly Monodisperse CdE (E = S, Se, Te) Semiconductor Nanocrystallites*, J. Am. Chem. Soc. **115**, 8706 (1993).

33. V. Biju, T. Itoh, A. Anas, A. Sujith, and M. Ishikawa, *Semiconductor quantum dots and metal nanoparticles: syntheses, optical properties, and biological applications*, Anal. Bioanal. Chem. **391**, 2469 (2008).

34. P. Buffat and J.-P. Borel, *Size effects on the melting temperature of gold particles*, Phys. Rev. A **13**, 2287 (1976).

35. A. A. Shvartsburg and M. F. Jarrold, *Solid Clusters above the Bulk Melting Point*, Phys. Rev. Lett. **85**, 2530 (2000).

36. K. Joshi, D. G. Kanhere, and S. A. Blundell, *Abnormally high melting temperature of the Sn_{10} cluster*, Phys. Rev. B **66**, 155329 (2002).

37. S. Chacko, K. Joshi, D. G. Kanhere, and S. A. Blundell, *Why Do Gallium Clusters Have a Higher Melting Point than the Bulk?*, Phys. Rev. Lett. **92**, 135506 (2004).

38. G. Ouyang, X. Tan, C. X. Wang, and G. W. Yang, *Solid solubility limit in alloying nanoparticles*, Nanotechnology **17**, 4257 (2006).

39. N. T. Gladkikh and O. P. Kryshtal, *On the size dependence of the vacancy formation energy*, Functional materials **6**, 823 (1999).

40. W. H. Qi and M. P. Wang, *Size dependence of vacancy formation energy of metallic nanoparticles*, Physica B **334**, 432 (2003).

41. M. Müller and K. Albe, *Concentration of thermal vacancies in metallic nanoparticles*, Acta Mater. **55**, 3237 (2007).

42. E. O. Hall, *The deformation and ageing of mild steel: III Discussion of results*, Proc. Phys. Soc. Lond. B **64**, 747 (1951).

43. N. J. Petch, *The cleavage of polycrystals*, J. Iron Steel Inst. **174**, 25 (1953).

44. J. Schøtz, F. D. Di Tolla, and K. W. Jacobsen, *Softening of nanocrystalline metals at very small grain sizes*, Nature **391**, 561 (1998).

45. C. C. Koch and J. Narayan, in *Structure and Mechanical Properties of Nanophase Materials — Theory and Computer Simulations vs. Experiment*, Vol. 634 of *MRS Proceedings*, edited by D. Farkas, H. Kung, M. Mayo, H. V. Swygenhoven, and J. Weertman (MRS, Boston, 2001), p. B5.1.1.

46. W. W. Gerbericha, W. M. Mook, C. R. Perrey, C. B. Carter, M. I. Baskes, R. Mukherjee, A. Gidwani, J. Heberlein, P. H. McMurry, and S. L. Girshick, *Superhard silicon nanospheres*, J. Mech. Phys. Sol. **51**, 979 (2003).

47. W. M. Mook, J. D. Nowak, C. R. Perrey, C. B. Carter, R. Mukherjee, S. L. Girshick, P. H. McMurry, and W. W. Gerberich, *Compressive stress effects on nanoparticle modulus and fracture*, Phys. Rev. B **75**, 214112 (2007).

48. Z. W. Shan, G. Adesso, A. Cabot, M. P. Sherburne, S. A. S. Asif, O. L. Warren, D. C. Chrzan, A. M. Minor, and A. P. Alivisatos, *Ultrahigh stress and strain in hierarchically structured hollow nanoparticles*, Nature Materials **7**, 947 (2008).

49. M. P. Allen and D. J. Tildesley, *Computer Simulation of Liquids* (Oxford University Press, Oxford, England, 1989).

50. J. von Boehm, *Molekyylidynamiikkamenetelmä* (Otatieto, Helsinki, Finland, 2000).

51. A. R. Leach, *Molecular modelling: principles and applications*, 2nd ed. (Pearson Prentice Hall, Harlow, England, 2001).

52. K. Nordlund, *Molecular dynamics simulation of ion ranges in the 1–100 keV energy range*, Comp. Mat. Sci. **3**, 448 (1995).

53. K. Nordlund, M. Ghaly, R. S. Averback, M. Caturla, T. Diaz de la Rubia, and J. Tarus, *Defect production in collision cascades in elemental semiconductors and fcc metals*, Phys. Rev. B **57**, 7556 (1998).

54. M. Ghaly, K. Nordlund, and R. S. Averback, *Molecular dynamics investigations of surface damage produced by kiloelectronvolt self-bombardment of solids*, Phil. Mag. A **79**, 795 (1999).

55. M. Born and R. Oppenheimer, *Zur Quantentheorie der Molekeln*, Annalen der Physik **84**, (1927).

56. A. D. Mackerell, Jr., *Empirical Force Fields for Biological Macromolecules: Overview and Issues*, J. Comput. Chem. **25**, 1584 (2004).

57. D. W. Brenner, *The Art and Science of an Analytic Potential*, phys. stat. sol. (b) **217**, 23 (2000).

58. J. H. Li, X. D. Dai, S. H. Liang, K. Tai, Y. Kong, and B. Liu, *Interatomic potentials of the binary transition metal systems and some applications in materials physics*, Phys. Rep. **455**, 1 (2008).

59. M. W. Finnis, *Bond-order potentials through the ages*, Prog. Mater. Sci. **52**, 133 (2007).

60. K. Nordlund and S. L. Dudarev, *Interatomic potentials for simulating radiation damage effects in metals*, C. R. Physique **9**, 342 (2008).

61. M. S. Daw and M. I. Baskes, *Semiempirical, Quantum Mechanical Calculation of Hydrogen Embrittlement in Metals*, Phys. Rev. Lett. **50**, 1285 (1983).

62. M. S. Daw and M. I. Baskes, *Embedded-atom method: Derivation and application to impurities, surfaces, and other defects in metals*, Phys. Rev. B **29**, 6443 (1984).

63. K. Albe, K. Nordlund, and R. S. Averback, *Modeling the metal-semiconductor interaction: Analytical bond-order potential for platinum-carbon*, Phys. Rev. B **65**, 195124 (2002).

64. N. Juslin, P. Erhart, P. Träskelin, J. Nord, K. O. E. Henriksson, K. Nordlund, E. Salonen, and K. Albe, *Analytical interatomic potential for modeling nonequilibrium processes in the W-C-H system*, J. Appl. Phys. **98**, 123520 (2005).

65. M. Mrovec, M. Moseler, C. Elsässer, and P. Gumbsch, *Atomistic modeling of hydrocarbon systems using analytic bond-order potentials*, Prog. Mater. Sci. **52**, 230 (2007).

66. M. Müller, P. Erhart, and K. Albe, *Analytic bond-order potential for bcc and fcc iron — comparison with established embedded-atom method potentials*, J. Phys.: Condens. Matter **19**, 326220 (2007).

67. J. Nord, K. Albe, P. Erhart, and K. Nordlund, *Modelling of compound semiconductors: analytical bond-order potential for gallium, nitrogen and gallium nitride*, J. Phys.: Condens. Matter **15**, 5649 (2003).

68. C. Björkas, N. Juslin, H. Timko, K. Vörtler, K. Henriksson, and P. Erhart, *Development of interatomic potentials for Be, Be-C and Be-H*, (unpublished).

69. S. M. Foiles, M. I. Baskes, and M. S. Daw, *Embedded-atom-method functions for the fcc metals Cu, Ag, Au, Ni, Pd, and their alloys*, Phys. Rev. B **33**, 7983 (1986).

70. M. Müller, P. Erhart, and K. Albe, *Thermodynamics of $L1_0$ ordering in FePt nanoparticles studied by Monte Carlo simulations based on an analytic bond-order potential*, Phys. Rev. B **76**, 155412 (2007).

71. M. Müller, *Atomistic Computer Simulations of FePt Nanoparticles: Thermodynamic and Kinetic Properties*, Ph.D. thesis, Technische Universität Darmstadt, 2007.

72. J. F. Ziegler, J. P. Biersack, and U. Littmark, *The Stopping and Range of Ions in Matter* (Pergamon, New York, 1985).

73. J. le Page, D. R. Mason, C. P. Race, and W. M. C. Foulkes, *How good is damped molecular dynamics as a method to simulate radiation damage in metals?*, New J. Phys. **11**, 013004 (2009).

74. K. Nordlund, J. Wallenius, and L. Malerba, *Molecular dynamics simulations of threshold displacement energies in Fe*, Nucl. Instrum. Methods Phys. Res. B **246**, 322 (2006).

75. H. J. C. Berendsen, J. P. M. Postma, W. F. van Gunsteren, and J. R. Haak, *Molecular dynamics with coupling to an external bath*, J. Chem. Phys. **81**, 3684 (1984).

76. To be released under the GNU General Public License (v. 2) on the author's home page.

77. K. Nordlund and R. S. Averback, *Point defect movement and annealing in collision cascades*, Phys. Rev. B **56**, 2421 (1997).

78. J. D. Honeycutt and H. C. Andersen, *Molecular Dynamics Study of Melting and Freezing of Small Lennard-Jones Clusters*, J. Phys. Chem. **91**, 4950 (1987).

79. E. Mendez-Villuendas and R. K. Bowles, *Surface Nucleation in the Freezing of Gold Nanoparticles*, Phys. Rev. Lett. **98**, 185503 (2007).

80. K. Wegner, P. Piseri, H. V. Tafreshi, and P. Milani, *Cluster beam deposition: a tool for nanoscale science and technology*, J. Phys. D: Appl. Phys. **39**, R439 (2006).

81. P. Jensen, *Growth of nanostructures by cluster beam deposition: Experiments and simple models*, Rev. Mod. Phys. **71**, 1695 (1999).

82. I. Yamada, J. Matsuo, N. Toyoda, and A. Kirkpatrick, *Materials processing by gas cluster ion beams*, Mat. Sci. Eng. R **34**, 231 (2001).

83. A. Kirkpatrick, *Gas cluster ion beam applications and equipment*, Nucl. Instrum. Methods Phys. Res. B **206**, 830 (2003).

84. A. Awasthi, S. C. Hendy, P. Zoontjens, S. A. Brown, and F. Natali, *Molecular dynamics simulations of reflection and adhesion behavior in Lennard-Jones cluster deposition*, Phys. Rev. B **76**, 115437 (2007).

85. R. Reichel, J. G. Partridge, F. Natali, T. Matthewson, S. A. Brown, A. Lassesson, D. M. A. Mackenzie, A. I. Ayesh, K. C. Tee, A. Awasthi, and S. C. Hendy, *From the adhesion of atomic clusters to the fabrication of nanodevices*, Appl. Phys. Lett. **89**, 213105 (2006).

86. J. Samela and K. Nordlund, *Atomistic Simulation of the Transition from Atomistic to Macroscopic Cratering*, Phys. Rev. Lett. **101**, 027601 (2008).

87. K. Meinander and K. Nordlund, *Modeling of film growth by cluster deposition: The effect of size and energy*, Phys. Rev. B **79**, 235435 (2009).

88. M. Yeadon, M. Ghaly, J. C. Yang, R. S. Averback, and J. M. Gibson, *"Contact epitaxy" observed in supported nanoparticles*, Appl. Phys. Lett. **73**, 3208 (1998).

89. M. Hou, *A molecular dynamics evidence for enhanced cluster beam epitaxy*, Nucl. Instrum. Methods Phys. Res. B **135**, 501 (1998).

90. S.-C. Lee, B. D. Yu, D.-Y. Kim, and N. M. Hwang, *Effects of cluster size and substrate temperature on the homoepitaxial deposition of Au clusters*, J. Cryst. Growth **242**, 463 (2002).

91. K. Meinander, J. Frantz, K. Nordlund, and J. Keinonen, *Upper size limit of complete contact epitaxy*, Thin Solid Films **425**, 297 (2003).

92. R. W. Cahn, *Melting from within*, Nature **413**, 582 (2001).

93. M. Forsblom and G. Grimvall, *How superheated crystals melt*, Nature Materials **4**, 388 (2005).

94. F. Delogu, *On the relationship between the mechanical and the thermal instabilities of crystalline lattices*, Mat. Sci. Eng. A **403**, 48 (2005).

95. J. P. Hirth and J. Lothe, *Theory of dislocations*, 2nd ed. (Krieger Publishing Company, Malabar, Florida, 1992).

96. J. A. Zimmerman, H. Gao, and F. F. Abraham, *Generalized stacking fault energies for embedded atom FCC metals*, Modelling Simul. Mater. Sci. Eng. **8**, 103 (2000).

97. V. S. Kharlamov, E. E. Zhurkin, and M. Hou, *Atomic scale modelling of nanoscale Ni_3Al cluster beam deposition on Al, Ni and Ni_3Al (111) surfaces*, Nucl. Instrum. Methods Phys. Res. B **193**, 538 (2002).

98. K. Meinander, T. T. Järvi, and K. Nordlund, *Contact epitaxy in multiple cluster deposition*, Appl. Phys. Lett. **89**, 253109 (2006).

99. K. Meinander, K. Nordlund, and J. Keinonen, *Inherent surface roughening as a limiting factor in epitaxial cluster deposition*, Nucl. Instrum. Methods Phys. Res. B **228**, 69 (2005).

100. J. Frantz, M. Rusanen, K. Nordlund, and I. T. Koponen, *Evolution of Cu nanoclusters on Cu(100)*, J. Phys. Condens. Matt. **16**, 2995 (2004).

101. M. F. Castez and R. C. Salvarezza, *Modeling thermal decay of high-aspect-ratio nanostructures*, Appl. Phys. Lett. **94**, 053103 (2009).

102. A. V. Krasheninnikov and K. Nordlund, *Irradiation-induced effects in nanostructured materials*, (unpublished).

103. P. Jung, in *Production of atomic defects in metals*, Vol. 25 of *Landolt-Börnstein, New Series III*, edited by H. Ullmaier (Springer, Berlin, 1991), Chap. 1, pp. 1–87.

104. R. S. Averback, *Atomic displacement processes in irradiated metals*, J. Nucl. Mater. **216**, 49 (1994).

105. R. S. Averback and T. Diaz de la Rubia, in *Solid State Physics*, edited by H. Ehrenfest and F. Spaepen (Academic Press, New York, 1998), Vol. 51, pp. 281–402.

106. T. Bergen, A. Brenac, F. Chandezon, C. Guet, H. Lebius, A. Pesnelle, and B. Huber, *Stopping power and nano-particles: Collisions of ions in low charge states with metallic clusters*, Eur. Phys. J. D **14**, 317 (2001).

107. L. Adriaensen, F. Vangaever, and R. Gijbels, *Metal-Assisted Secondary Ion Mass Spectrometry: Influence of Ag and Au Deposition on Molecular Ion Yields*, Anal. Chem. **76**, 6777 (2004).

108. A. Marcus and N. Winograd, *Metal Nanoparticle Deposition for TOF-SIMS Signal Enhancement of Polymers*, Anal. Chem. **78**, 141 (2006).

109. Y.-P. Kim, E. Oh, H. K. Shon, D. W. Moon, T. G. Lee, and H.-S. Kim, *Gold nanoparticle-enhanced secondary ion mass spectrometry and its bio-applications*, Appl. Surf. Sci. **255**, 1064 (2008).

110. R. Kissel and H. M. Urbassek, *Sputtering from spherical Au clusters by energetic atom bombardment*, Nucl. Instrum. Methods Phys. Res. B **180**, 293 (2001).

111. P. Sigmund, in *Sputtering by Particle Bombardment I*, Vol. 47 of *Topics in Applied Physics*, edited by R. Behrisch (Springer-Verlag, Berlin, 1981), Chap. 2, pp. 9–71.

112. J. F. Ziegler, SRIM-2008 software package, available online at *www.srim.org*.

113. G. B. Arfken and H. J. Weber, *Mathematical methods for physicists* (Academic Press, San Diego, California, 1995).

114. A. Klimmer, P. Ziemann, J. Biskupek, U. Kaiser, and M. Flesch, *Size-dependent effect of ion bombardment on Au nanoparticles on top of various substrates: Thermodynamically dominated capillary forces versus sputtering*, Phys. Rev. B **79**, 155427 (2009).

115. P. Ehrhart, K. H. Robrock, and H. R. Schober, in *Physics of Radiation Effects in Crystals*, edited by R. A. Johnson and A. N. Orlov (Elsevier Science Publishers B. V., North-Holland, Amsterdam, 1986), Chap. 1, pp. 3–115.

116. G. Kinchin and R. Pease, *The displacement of atoms in solids by radiation*, Rep. Prog. Phys. **18**, 1 (1955).

117. M. J. Norgett, M. T. Robinson, and I. M. Torrens, *A proposed method of calculating displacement dose rates*, Nucl. Eng. Des. **33**, 50 (1975).

118. J. Paulevé, D. Dautreppe, J. Laugier, and L. Néel, *Physique cristalline — Etablissement d'une structure ordonnée FeNi par irradiation aux neutrons*, C. R. Acad. Sci. (Paris) **254**, 965 (1962).

119. H. Bernas, J.-P. Attané, K.-H. Heinig, D. Halley, D. Ravelosona, A. Marty, P. Auric, C. Chappert, and Y. Samson, *Ordering Intermetallic Alloys by Ion Irradiation: A Way to Tailor Magnetic Media.*, Phys. Rev. Lett **91**, 077203 (2003).

120. C. Uzan-Saguy, C. Cytermann, R. Brener, V. Richter, M. Shaanan, and R. Kalish, *Damage threshold for ion-beam induced graphitization of diamond*, Appl. Phys. Lett. **67**, 1194 (1995).

121. A. T. Motta, *Amorphization of intermetallic compounds under irradiation - A review*, J. Nucl. Mater. **244**, 227 (1997).

122. K. Trachenko, *Understanding resistance to amorphization by radiation damage*, J. Phys.: Condens. Matter **16**, R1491 (2004).

123. S. Talapatra, J.-Y. Cheng, N. Chakrapani, S. Trasobares, A. Cao, R. Vajtai, M. B. Huang, and P. M. Ajayan, *Ion irradiation induced structural modifications in diamond nanoparticles*, Nanotechnology **17**, 305 (2006).

124. G. Mattei, C. Maurizio, C. de Julián Fernández, P. Mazzoldi, G. Battaglin, P. Canton, E. Cattaruzza, and C. Scian, *Size dependent hcp-to-fcc transition temperature in Co nanoclusters obtained by ion implantation in silica*, Nucl. Instrum. Methods Phys. Res. B **250**, 206 (2006).

125. N. V. Seetala, J. W. Harrell, J. Lawson, D. E. Nikles, J. R. Williams, and T. Isaacs-Smith, *Ion-irradiation induced chemical ordering of FePt and FePtAu nanoparticles*, Nucl. Instrum. Methods Phys. Res. B **241**, 583 (2005).

126. Y. Ding and S. A. Majetich, *Size dependence, nucleation, and phase transformation of FePt nanoparticles*, Appl. Phys. Lett. **87**, 022508 (2005).

127. U. Wiedwald, A. Klimmer, B. Kern, L. Han, H.-G. Boyen, P. Ziemann, and K. Fauth, *Lowering of the $L1_0$ ordering temperature of FePt nanoparticles by He^+ ion irradiation*, Appl. Phys. Lett. **90**, 062508 (2007).

128. K. Yano, V. Nandwana, N. Poudyal, C.-B. Rong, and J. P. Liu, *Rapid thermal annealing of FePt nanoparticles*, J. Appl. Phys. **104**, 013918 (2008).

129. B. Rellinghaus, E. Mohn, L. Schultz, T. Gemming, M. Acet, A. Kowalik, and B. F. Kock, *On the $L1_0$ Ordering Kinetics in Fe-Pt Nanoparticles*, IEEE T. Magn. **42**, 3048 (2006).

130. M. Müller and K. Albe, *Lattice Monte Carlo simulations of FePt nanoparticles: Influence of size, composition, and surface segregation on order-disorder phenomena*, Phys. Rev. B **72**, 094203 (2005).

131. B. Yang, M. Asta, O. N. Mryasov, T. J. Klemmer, and R. W. Chantrell, *The nature of A1-$L1_0$ ordering transition in alloy nanoparticles: A Monte Carlo study*, Acta Mater. **54**, 4201 (2006).

132. O. Dmitrieva, B. Rellinghaus, J. Kästner, M. O. Liedke, and J. Fassbender, *Ion beam induced destabilization of icosahedral structures in gas phase prepared FePt nanoparticles*, J. Appl. Phys **97**, 10N112 (2005).

133. C. L. Cleveland, U. Landman, and W. D. Luedtke, *Phase Coexistence in Clusters*, J. Phys. Chem. **98**, 6272 (1994).

134. S. Stappert, B. Rellinghaus, M. Acet, and E. F. Wassermann, *Gas-phase preparation of $L1_0$ ordered FePt nanoparticles*, J. Cryst. Growth **252**, 440 (2003).

135. M. L. Jenkins and C. A. English, *Characterization of displacement cascade damage in ordered alloys using transmission electron microscopy*, J. Nucl. Mat. **108–109**, 46 (1982).

136. V. A. Ivchenko and N. N. Syutkin, *Effect of low-energy (20–40 keV) ion implantation on phase transformations in the subsurface volume of alloys*, Appl. Surf. Sci. **87–88**, 257 (1995).

137. G. Battaglin, A. Carnera, V. N. Kulkarni, S. L. Russo, P. Mazzoldi, and G. Celotti, *Extended solid solution of iron in platinum by ion beam mixing: Role of energy deposition and effect of thermal treatment*, Thin Solid Films **131**, 69 (1985).

138. N. W. Morgan, R. C. Birtcher, and G. B. Thompson, *In situ transmission electron microscopy of ion irradiated Fe-Pt alloy thin films*, J. Appl. Phys. **100**, 124904 (2006).

139. E. Goo, A. Murthy, and C. J. D. Hetherington, *Preferential amorphization of NiTi alloys at twin boundaries by electron irradiation*, Scr. Metall. Mater. **29**, 553 (1993).

140. A. Meldrum, L. A. Boatner, and R. C. Ewing, *Nanocrystalline Zirconia Can Be Amorphized by Ion Irradiation*, Phys. Rev. Lett. **88**, 025503 (2002).

141. M. Backman, F. Djurabekova, O. H. Pakarinen, K. Nordlund, L. L. Araujo, and M. C. Ridgway, *Amorphization of Ge and Si nanocrystals embedded in amorphous SiO_2 by ion irradiation*, Phys. Rev. B (in press).

142. B. Johannessen, P. Kluth, D. J. Liewellyn, G. J. Foran, D. J. Cookson, and M. C. Ridgway, *Amorphization of embedded Cu nanocrystals by ion irradiation*, Appl. Phys. Lett. **90**, 073119 (2007).